Front. Energy 2019, 13(2): 221–250
https://doi.org/10.1007/s11708-019-0629-8

REVIEW ARTICLE

Lei ZHANG, Junqing ZHANG

Metal-organic frameworks for CO_2 photoreduction

Abstract Metal-organic frameworks (MOFs) have attracted much attention because of their large surface areas, tunable structures, and potential applications in many areas. In recent years, MOFs have shown much promise in CO_2 photoreduction. This review summarized recent research progresses in MOF-based photocatalysts for photocatalytic reduction of CO_2. Besides, it discussed strategies in rational design of MOF-based photocatalysts (functionalized pristine MOFs, MOF-photosensitizer, MOF-semiconductor, MOF-metal, and MOF-carbon materials composites) with enhanced performance on CO_2 reduction. Moreover, it explored challenges and outlook on using MOF-based photocatalysts for CO_2 reduction.

Keywords metal-organic frameworks (MOFs), photocatalysis, CO_2 photoreduction, composite

1 Introduction

Carbon dioxide (CO_2) released in the combustion of fossil fuels, such as oil, coal, and natural gas, makes up the majority of greenhouse gas emissions, which is the major contributor to global warming [1,2]. Therefore, it is imperative to develop technologies to reduce CO_2 emissions. To date, the main approaches developed to reduce CO_2 emissions include ① CO_2 capture and sequestration and ② CO_2 conversion and utilization. CO_2 capture and sequestration is a set of technologies developed for reducing CO_2 emissions from fossil-fueled power plants. CO_2 capture is to separate CO_2 from gas mixtures via chemical absorption using an agent such as monoethanol amine or physical adsorption using solid adsorbents such as activated carbons and metal organic frameworks (MOFs), membrane separation and cryogenic separation at a low temperature [3]. CO_2 sequestration refers to long-term storage of CO_2 in ocean, soils, plants, and geologic formations [3,4]. However, these technologies are relatively energy-intensive and thus are not cost-effective. An alternative sustainable approach to mitigating CO_2 emissions is CO_2 utilization and conversion. CO_2 utilization describes the uses of CO_2 in both physical processes such as welding medium and chemical processes such as chemical synthesis. The CO_2 utilization technology has found applications in several industries such as carbonated drinks, dry ice, solvent, food preservation, refrigerant, and fire extinguisher. These direct CO_2 utilization applications, however, have a small effect on the overall CO_2 emission reduction due to the limited usage [5]. CO_2 utilization can also be employed indirectly in industries to promote a process such as in enhanced gas recovery, enhanced oil recovery, and enhanced geothermal systems. CO_2 conversion refers to the transformation of CO_2 into valuable products such as fuels and chemicals. CO_2 can be utilized directly as a feedstock to react with other components to form chemical products such as urea and formic acid under heat and/or pressure. CO_2 can also be utilized indirectly as a building block of a chemical product [6]. It is worth noting that CO_2 is a highly stable molecule. The C–O bond strength in CO_2 molecule is 364 kJ/mol and the carbon atom has the highest oxidation state, therefore, CO_2 conversion into valuable chemicals generally requires a significant input of energy and the use of a catalyst [7]. The main approaches to converting CO_2 into valuable products include photocatalysis [8,9], chemical fixation [10], hydrogenation [11], and electrocatalysis [12]. Among these methods, photocatalytic reduction of CO_2 attracts much attention because it converts CO_2 into useful products by utilizing solar energy via a clean and sustainable route. Under sunlight irradiation, photocatalysts can induce CO_2 reduction and convert it into fuels and chemicals, mainly including CO, HCHO, HCOOH, CH_3OH, C_2H_5OH, and CH_4, etc., which is determined by the number of electrons and protons (e^-/H^+) transferred in the reactions. The selectivity of product and efficiency of CO_2 reduction may have been affected by the thermodynamic reduction potentials and reaction conditions. H_2O

Received Dec. 17, 2018; accepted Feb. 23, 2019; online May 30, 2019

Lei ZHANG (✉), Junqing ZHANG (✉)
Department of Mechanical Engineering, University of Alaska Fairbanks, Fairbanks, AK 99775, USA
E-mails: lzhang14@alaska.edu; jzhang16@alaska.edu

is commonly used as a solvent for CO_2 photocatalytic reduction because it is of low cost and is natural abundance of hydrogen. The photoreduction reactions of CO_2 in aqueous solution at pH = 7 and their reduction potentials with reference to the normal hydrogen electrode (NHE) at 25°C and 1 atm are given in Table 1 [13,14].

Table 1 Photoreduction reactions of CO_2 in aqueous solution at pH = 7 and their reduction potentials with reference to normal hydrogen electrode (NHE) at 25°C and 1 atm

Reaction	Thermodynamics potential (V) vs. NHE
$CO_2 + 2H^+ + 2e^- \rightarrow HCOOH$	−0.61
$CO_2 + 4H^+ + 4e^- \rightarrow HCHO + H_2O$	−0.52
$CO_2 + 2H^+ + 2e^- \rightarrow CO + H_2O$	−0.48
$CO_2 + 6H^+ + 6e^- \rightarrow CH_3OH + H_2O$	−0.38
$CO_2 + 8H^+ + 8e^- \rightarrow CH_4 + 2H_2O$	−0.24
$H_2O \rightarrow 1/2O_2 + 2H^+ + 2e^-$	+0.82
$2H^+ + 2e^- \rightarrow H_2$	−0.41

Photocatalysis is a process that converts solar energy to chemical energy, where solar energy is the driving force for the excitation and transfer of holes and electrons to induce oxidation and reduction reactions. The photocatalytic CO_2 reduction process can be explained as follows: first, under light illumination with energy greater than the band gap of the photocatalysts, electrons are excited from the valence band (VB) to the conduction band (CB), generating an equal number of holes in the VB. Secondly, electron-hole pairs separate from each other and move to the surface of photocatalyst. Finally, the electrons reduce CO_2 into chemical products, while the holes oxidize a sacrificial agent or H_2O. To induce CO_2 photoreduction, it requires that reduction potential and oxidation potential of the reaction is less negative and less positive than the CB edge and the VB edge of the photocatalyst, respectively.

Since Fujishima et al. reported on the feasibility of using TiO_2 for photoelectron chemical water splitting under ultraviolet (UV) irradiation [15], many different photocatalysts have been developed, most of which are inorganic semiconductors such as TiO_2 [16], CdS [17], ZnO [18], ZnS [19], Fe_2O_3 [20], g-C_3N_4 [21], Ag_3PO_4 [22] and their composites. Some cocatalysts such as Pt have also been explored [23,24]. However, the wide band gap, high recombination rate of electron-hole pairs, low adsorption capacities for CO_2, and less tunable structure of the conventional semiconductors limit their practical applications. For example, TiO_2 is mainly used for UV light photocatalysis because of its wide band gap (3–3.2 eV) [25]. ZnO and CdS are not stable under irradiation in an aqueous solution, making them inactive over time [26,27]. Therefore, it is imperative to develop new photocatalytic materials with finely tunable energy band structures and high stability.

Metal-organic frameworks (MOFs), a new class of inorganic-organic hybrid material composed of inorganic metal clusters and organic linkers which are connected through coordination bonds, have attracted much interest due to their large surface areas, tunable structures and high porosity [28–34]. These excellent properties enable their wide applications in many fields, such as gas storage and separation [35], catalysis [36], drug delivery [37], water treatments [38], and sensing [39]. Recently, MOFs have found applications in CO_2 photoreduction, degradation of organics, and chemical synthesis as photocatalytic materials [40–42]. In photocatalytic reaction, MOFs undergo a similar process to traditional semiconductors, but differently, the VB and CB are described as the highest occupied molecular orbital (HOMO) and the lowest unoccupied molecular orbital (LUMO) in MOFs, respectively [36,43]. In general, the HOMO and LUMO energy levels are associated with the redox potential energy levels of the organic linker and the metal-oxo cluster, respectively [42]. The tunable organic linkers and/or metal clusters in MOFs can act as antennas to harvest light to generate electron-hole pairs for photocatalysis. Most of the photocatalytic reactions in MOFs reported to date are ascribed to a localized metal-to-ligand charge transfer (MLCT), a ligand-to-metal charge transfer (LMCT), or a π–π^* transition of the aromatic ligand [36]. MOFs are utilized for photocatalytic reduction of CO_2 because of their attributes as follows: ① both the organic linkers and metal clusters can serve as the light harvesting sites and they can be tailored to tune the optical absorption range of MOFs [44], ② some MOFs have a catalytic activity resulting from the catalytically active organic linkers and/or unsaturated metal sites [45,46], ③ MOFs have a large surface area and a high CO_2 adsorption capacity, and the high CO_2 concentration in the pores can facilitate the photocatalytic reactions, and ④ the three-dimensional porous structures and high surface areas enable MOFs to incorporate foreign photoactive species into their frame works, through which photocatalytic reactions can be enhanced by the synergistic cooperation of the metal clusters, organic linkers and the incorporated active sites [47]. Based on these unique properties, MOFs are promising photocatalysts for CO_2 reduction.

MOF photocatalysts can be classified into two categories: ① Pristine MOF photocatalysts, which are also called “opportunistic” photocatalysts. The photocatalytic properties of some pristine MOFs are a consequence of the catalytically active organic linkers and unsaturated metal sites [48], and some MOFs are semiconductors [49–51] whose photocatalytic reactions are completed through LMCT. Most pristine MOFs as photocatalysts, however, have large band gaps and barely absorb visible light, which limits their practical applications. These MOFs generally have a low photon energy utilization efficiency, and are typically employed for photocatalytic degradation of organics which have high thermodynamic driving forces

and low kinetic barriers [36]. ② Modified MOF photocatalysts, which refer to MOFs functionalized to increase light harvesting and decrease the recombination rate of the photo-generated charge carriers for photocatalytic activity enhancement. To date, many strategies have been developed for enhancing the photocatalytic properties of MOFs under solar illumination, including the decoration of the metal clusters and organic linkers [52,53], incorporation of foreign photocatalytic species such as metal particles, semiconductors [54–56], and photosensitizers [57–59].

So far, a number of good literature reviews have summarized the photocatalytic applications of MOFs [60–69], most of which have discussed the role of MOFs and their performances in water splitting [70–73], degradation of organic pollutants [74–77], hydrogen evolution [36,78–80], and CO_2 conversion [36,43,66,78,80–85]. Therefore, this review is mainly focused on reviewing the recent progresses of MOF-based photocatalysts in CO_2 photoreduction. Besides, it discusses modification strategies of MOFs and their photocatalytic activities in CO_2 reduction. Moreover, it explores the challenges and future perspectives of MOFs-based photocatalysts in CO_2 photoreduction.

2 Modification of pristine MOFs as photocatalysts

Compared to traditional inorganic semiconductors, it is more convenient to tune the optical properties and consequently the photocatalytic properties of MOFs by modification of the metal clusters or organic linkers. It is reported that the linker decoration can change the energy band gap of MOFs by shifting the photo absorption edge from the UV to visible light region [86]. Many strategies have been developed to functionalize organic linkers and metal clusters [44,87–92], such as amine and photosensitizer functionalization of organic linkers and incorporation of foreign metal cations into organic linkers and metal sites (e.g., Ti–O, Fe–O, and Zr–O clusters). The performances of recent photocatalytic MOFs for CO_2 photoreduction are summarized in Table 2.

2.1 Metal cluster nodes

MOFs have three-dimensional structures constructed from the interconnection of metal cluster nodes with organic linkers. Besides photoactive ligands, metal cluster nodes in MOFs can also drive photocatalytic CO_2 reduction. To date, Ti-, Zr-, and Fe-based MOFs are among the most investigated photocatalytic MOFs whose photoactive metal nodes in metal-oxo clusters can initiate photocatalytic reaction by trapping photo-excited electrons and decreasing recombination rate of electron-hole pairs [83]. These MOFs share the similarity that they all contain metal ions with variable valence states (e.g., Ti^{4+}/Ti^{3+}, Zr^{4+}/Zr^{3+} , and Fe^{3+}/Fe^{2+}), which enables their effectiveness on photocatalytic reduction.

Of the Ti-based MOFs, MIL-125(Ti) ($Ti_8O_8(OH)_4(O_2C\text{-}C_6H_4\text{-}CO_2)_6$) is the most studied MOF, which is constructed from the $Ti_8O_8(OH)_4$ secondary building units (SBUs) and 1,4-benzenediacarboxylate (BDC) ligands. Fu et al. investigated the CO_2 photoreduction over MIL-125(Ti) [53]. 2.41 μmol $HCOO^-$ was detected in the acetonitrile (MeCN) solvent with TEOA under 365 nm UV light irradiation for 10 h. A number of strategies have been developed to functionalize MIL-125(Ti) to enhance the photocatalytic reduction of CO_2, such as organic linker decoration and incorporation of foreign photocatalytic components into MOFs to form MOF composites. These strategies will be discussed in Section 2.2 and Section 3.

Zr-based MOFs, which have robust structures and excellent thermal and chemical stabilities [112,113], are another popular class of photocatalytic MOFs since their synthesis in 2008 [114]. The representative examples are UiO-66(Zr) and UiO-67(Zr), which are constructed by integrating $Zr_6O_4(OH)_4$ SBUs with BDC ligands and 4,4′-biphenyldicarboxylic acid (BPDC) ligands, respectively [114,115]. Compared to Ti-based MOFs, Zr-based MOFs have more negative redox potential (Ti^{4+}/Ti^{3+} (–0.1 V), Zr^{4+}/Zr^{3+} (–1.06 V)) [116,117]. However, UiO-66 exhibits no absorption under visible light irradiation owing to the higher redox potential energy level of the $Zr_6O_4(OH)_4$ SBUs in UiO-66 than the LUMO of the BDC linkers, leading to the low efficiency in LMCT and consequently low efficacy in CO_2 photoreduction [94]. Partial substitution of metal cations in MOFs can introduce metal-to-metal charge transfer, which can promote photocatalytic performance especially under visible light irradiation [94,96]. A bimetallic UiO-based MOF, NH_2-UiO-66(Zr/Ti), was prepared by Cohen and coworkers by partially substituting Zr in NH_2-UiO-66(Zr) with Ti [94]. NH_2-UiO-66(Zr/Ti) had a better performance in photocatalytic CO_2 reduction under visible light irradiation compared to NH_2-UiO-66 (Zr). The reason for this is that Ti ions incorporated enable the SBUs to accept the electrons generated via light absorption by the organic linkers. No $HCOO^-$ was produced over the parent UiO-66(Zr)-NH_2, demonstrating that Ti was critical for photocatalysis.

Sun et al. also prepared Ti-substituted NH_2-UiO-66(Zr/Ti) MOFs (NH_2-UiO-66(Zr/Ti)-120-16 and NH_2-UiO-66 (Zr/Ti)-100-4) doped with different amounts of Ti by a post-synthetic exchange method and examined their photocatalytic performance on CO_2 reduction under visible light irradiation (Fig. 1(a)) [96]. NH_2-UiO-66(Zr/Ti)-120-16 had an enhanced photocatalytic activity toward CO_2 conversion with a yield of 5.8 mmol/mol of $HCOO^-$ after 10 h visible light irradiation in MeCN solvent with TEOA as a sacrificial agent, which was 1.7 times of that observed over NH_2-UiO-66(Zr) (3.4 mmol/mol) under similar conditions. In contrast, NH_2-UiO-66(Zr/Ti)-100-4 produced 4.2 mmol/mol of $HCOO^-$, which was less than NH_2-

Table 2 Performances of recent photocatalytic MOFs for CO_2 photoreduction

Functionalization	MOF	Irradiation	Solvent/sacrificial agent	Main product	Photocatalytic reactivity	Reaction time/h	Ref.
–	MIL-125(Ti)	UV	MeCN/TEOA	$HCOO^-$	2.41 μmol	10	[53]
–	MIL-125(Ti)	Visible			0		
NH_2-functionalized linker	MIL-125(Ti)-NH_2				8.14 μmol		
NH_2-functionalized linker	NH_2-UiO-66(Zr)	Visible	MeCN/TEOA	$HCOO^-$	13.2 μmol	10	[93]
	$(NH_2)_2$-UiO-66(Zr)				20.7 μmol		
NH_2-modified with partial Ti cation substitution	NH_2-UiO-66(Zr/Ti)	Visible	MeCN/TEOA BNAH	$HCOO^-$	22.23 μmol	6	[94]
	$(NH_2)_2$-UiO-66(Zr/Ti)				31.57±1.64 μmol		
–	MIL-101(Fe)	Visible	MeCN/TEOA	$HCOO^-$	59.0 μmol	8	[95]
NH_2-functionalized linker	MIL-101(Fe)-NH_2				178 μmol		
–	MIL-53(Fe)				29.7 μmol		
NH_2-functionalized linker	MIL-53(Fe)-NH_2				46.5 μmol		
–	MIL-88B(Fe)				9.0 μmol		
NH_2-modified with partial metal ion substitution	MIL-88B(Fe)-NH_2				30 μmol		
NH_2-modified with partial Ti cation substitution	NH_2-UiO-66(Zr/Ti)	Visible	MeCN/TEOA	$HCOO^-$	3.4 mmol/mol	10	[96]
	NH_2-UiO-66(Zr/Ti)-100-4				4.2 mmol/mol		
	NH_2-UiO-66(Zr/Ti)-120-16				5.8 mmol/mol		
Porphyrin- functionalized linker	Rh-PMOF-1(Zr)	Visible	MeCN/TEOA	$HCOO^-$	6.1 μmol/μmol	18	[97]
Porphyrin- functionalized linker	Zn/PMOF	UV-visible	H_2O vapor	CH_4	10.43 μmol	4	[98]
Porphyrin- functionalized linker	Al/PMOF	Visible	H_2O/TEOA	CH_3OH	37.5 ppm /(g·h)	–	[99]
Porphyrin- functionalized linker with partial Cu cation substitution	Cu-Al/PMOF				262.6 ppm /(g·h)		
Porphyrin- functionalized linker	MOF-525	Visible	MeCN/TEOA	CO	64.02 μmol /(g·h)	6	[100]
				CH_4	6.2 μmol /(g·h)		

(*Continued*)

Functionalization	MOF	Irradiation	Solvent/sacrificial agent	Main product	Photocatalytic reactivity	Reaction time/h	Ref.
Porphyrin- functionalized linker with embedded Zn cations	MOF-525-Zn			CO	111.7 μmol /(g·h)		
				CH_4	11.64 μmol /(g·h)		
Porphyrin- functionalized linker with embedded Co cations	MOF-525-Co			CO	200.6 μmol /(g·h)		
				CH_4	36.76 μmol /(g·h)		
Porphyrin- functionalized linker	PCN-222	Visible	MeCN/TEOA	$HCOO^-$	30 μmol	10	[101]
Photosensitizer functionalization	Eu-Ru(phen)$_3$-MOF	Visible	MeCN/TEA	$HCOO^-$	47 μmol	10	[102]
Photosensitizer functionalization	UiO-67-$Re^I(CO)_3$(5,5′-dcbpy)Cl	Visible	MeCN/TEA	CO	TON = 5.0	6	[103]
				H_2	TON = 0.5		
				CO	TON = 10.9	20	
				H_2	TON = 2.5		
–	$Re^I(CO)_3$(5,5′-dcbpy)Cl			CO	TON = 5.6	6	
				H_2	TON = 0.3		
				CO	TON = 7.0	20	
				H_2	TON = 1.0		
Photosensitizer functionalization	$Zr_6(O)_4(OH)_4[Re(CO)_3Cl(bpydb)]_6$	Visible	MeCN/TEA	CO	TON = 6.44	6	[104]
				H_2	TON = 0.40	6	
Photosensitizer functionalization	UiO-67-$Re^I(CO)_3$(5,5′-dcbpy)Cl	Visible	TEA	CO	0.5 μmol/(g·h)	6	[52]
	UiO-67-$Re^I(CO)_3$(5,5′-dcbpy)Cl–NH_2 (33% (mol))			CO	1.5 μmol/(g·h)	6	
Photosensitizer functionalization	UiO-67-Cp*Rh(5,5′- dcbpy)Cl_2 (10%)	Visible	ACN/TEOA	$HCOO^-$	TON = 47	10	[105]
				H_2	TON = 36		
–	Cp*Rh(5,5′- dcbpy)Cl_2			$HCOO^-$	TON = 42		
				H_2	TON = 38		
–	[Ru(bpy)$_3$]Cl_2			$HCOO^-$	TON = 125		
				H_2	TON = 55		
Photosensitizer functionalization	MOF-253-Ru(CO)$_2Cl_2$	Visible	MeCN/TEOA	$HCOO^-$	0.67 μmol	8	[106]
				CO	1.86 μmol		
				H_2	0.09 μmol		

(*Continued*)

Functionalization	MOF	Irradiation	Solvent/sacrificial agent	Main product	Photocatalytic reactivity	Reaction time/h	Ref.
	$Ru(bpy)_2Cl_2$- sensitized MOF-253-Ru $(CO)_2Cl_2$			$HCOO^-$	4.84 μmol		
				CO	1.85 μmol		
				H_2	0.72 μmol		
	MOF-253-$Ru(bpy)_2Cl_2$			$HCOO^-$	0.46 μmol		
				CO	0.21 μmol		
				H_2	0.07 μmol		
–	$Ru(bpy)_2Cl_2$			$HCOO^-$	0.27 μmol		
				CO	0.18 μmol		
				H_2	0 μmol		
Photosensitizer functionalization	$Y[Ir(ppy)_2(4,4'\text{-dcbpy})]_2[OH]$	Visible	MeCN/TEOA	$HCOO^-$	118.8 μmol/(g·h)	6	[107]
Photosensitizer functionalization	$[Cd_2[Ru(4,4'\text{-dcbpy})_3]\cdot 12H_2O]_n$ nano-flower	Visible	MeCN/TEOA	$HCOO^-$	77.2 μmol/(g·h)	8	[108]
	$[Cd_2[Ru(4,4'\text{-dcbpy})_3]\cdot 12H_2O]_n$ micro-flake				52.7 μmol/(g·h)		
	$[Cd_2[Ru(4,4'\text{-dcbpy})_3]\cdot 12H_2O]_n$ bulk crystals				30.6 μmol/(g·h)		
Photosensitizer functionalization	$[Cd_3[Ru(5,5'\text{-dcbpy})_3]_2\cdot 2(Me_2NH_2)]_n$	Visible	MeCN/TEOA	$HCOO^-$	67.5 μmol/(g·h)	6	[109]
	$[Cd[Ru(bpy)(4,4'\text{-dcbpy})_2]\cdot 3H_2O]_n$				71.7 μmol/(g·h)		
Catechol- functionalized linker	UiO-66-Cr^{III}catbdc	Visible	MeCN/TEOA/BNAH	$HCOO^-$	TON = 11.22±0.37	6	[110]
	UiO-66-Ga^{III}catbdc				TON = 6.14±0.22		
Anthracene- functionalized linker	NNU-28	Visible	MeCN/TEOA	$HCOO^-$	183.3 μmol/(h·mmol)	10	[111]

Notes: ACN–acetonitrile; BNAH–1-benzyl-1,4-dihydronicotinamide; bpy–2,2'-bipyridine; catbdc–2,3-dihydroxyterephthalic acid; Cp*–pentamethylcyclopentadiene; MeCN–acetonitrile; phen–phenanthroline; TEA–trimethylamine; TEOA–triethanolamine; TON–total turnover number; 5,5′-dcbpy–2,2'-bipyridine-5,5′-dicarboxylic acid; bpydb–4,4'-(2,2'-bipyridine-5,5′-diyl)dibenzoate; ppy–2-phenylpyridine; 4,4'-dcbpy–2,2'-bipyridine-4,4'-dicarboxylate

UiO-66(Zr/Ti)-120-16, but still higher than that over the pristine NH_2-UiO-66(Zr). The enhancement in photocatalytic performance over Ti-substituted NH_2-UiO-66(Zr/Ti) MOFs is associated with the increase in CO_2 adsorption capacity and photocatalytic sites, both of which result from Ti doped into Zr-O clusters of NH_2-UiO-66(Zr). Based on the experimental observations and theoretical studies, the mechanism for enhanced photocatalytic reactions over NH_2-UiO-66(Zr/Ti) is proposed (see Fig. 1(b)). When Zr^{4+} centers in $Zr_6O_4(OH)_4$ are partially substituted by Ti^{4+} to form $(Ti/Zr)_6O_4(OH)_4$, the excited NH_2-BDC upon visible light irradiation can transfer electrons to either Zr^{4+} or Ti^{4+} centers. The theoretical calculations show that there is a higher probability for electrons to be transferred to Ti^{4+} than that to Zr^{4+} centers, leading to the formation of $(Ti^{3+}/Zr^{4+})_6O_4(OH)_4$ SBUs. The Ti^{3+} in the excited $(Ti^{3+}/Zr^{4+})_6O_4(OH)_4$ SBUs can play a role of electron donor to donate electrons to Zr^{4+}, leading to Ti^{4+}–O–Zr^{3+} formation. As a result, the substituted Ti center in NH_2-UiO-66(Zr/Ti) facilitates the interfacial charge transfer from the excited NH_2-BDC to Zr–O clusters, which boosts the enhanced photocatalytic reactions over NH_2-UiO-66(Zr/Ti).

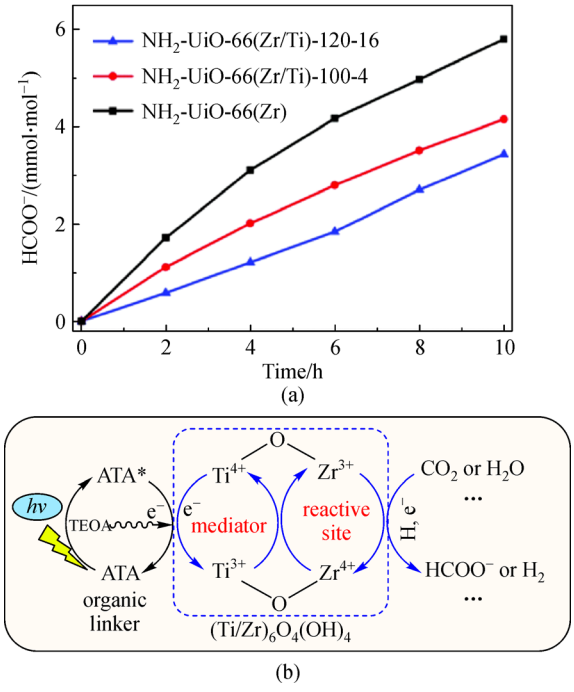

Fig. 1 Enhanced photoreduction of CO_2 over NH_2-UiO-66(Zr) induced by Ti substitution and the proposed CO_2 photoreduction mechanism

(a) Amount of $HCOO^-$ produced over different samples as a function of light irradiation time; (b) proposed mechanism for the CO_2 photoreduction over NH_2-UiO-66(Zr/Ti) (Reproduced with permission from Ref. [96]. Copyright 2015, Royal Society of Chemistry)

Recently, Fe-based MOFs as photocatalysts for CO_2 reduction have attracted much interest owing to the fact that the Fe–O clusters can be directly photoexcited to induce electron transfer from O^{2-} to Fe^{3+} to form Fe^{2+} under visible light irradiation, which drives the photocatalytic reaction [95,118]. Since the Fe sites play a role of photocatalytic centers, Fe-based MOFs are capable of photocatalytically reducing CO_2 under visible light irradiation in the absence of LMCT. Wang et al. reported a series of Fe-based MOFs, MIL-101(Fe), MIL-53(Fe), MIL-88B(Fe), all of which had a photocatalytic activity for CO_2 reduction to produce $HCOO^-$ under visible light irradiation [95]. It showed that the photocatalytic activity of MIL-101(Fe), MIL-53(Fe) and MIL-88B(Fe) toward CO_2 conversion into $HCOO^-$ in MeCN solvent with TEOA as a sacrificial reactant was 59.0, 29.7, and 9.0 μmol, respectively, after visible light irradiation for 8 h. Of the three investigated Fe-based MOFs, MIL-101(Fe) had the best photocatalytic performance attributing to the existence of the unsaturated Fe sites in its structure that were absent in MIL-53(Fe) and MIL-88B(Fe). MIL-53(Fe) had a better activity than MIL-88B(Fe) attributing to its higher CO_2 adsorption capacity (13.5 g/cm^3) than MIL-88B(Fe) (10.4 g/cm^3) which might be ascribed to its one dimensional framework structure which possessed a better electroconductivity. The photocatalytic activities of the three Fe-based MOFs were enhanced by amine functionalization. The $HCOO^-$ yield of 178, 46.5, and 30 μmol was produced over NH_2-MIL-101(Fe), NH_2-MIL-53(Fe), and NH_2-MIL-88B(Fe), respectively, under the same photocatalytic conditions, which were higher in comparison to the parent Fe-MOFs. This photocatalytic activity enhancement is caused by the existence of the dual excitation pathways: excitation of NH_2-functionalized organic ligands to transfer electrons to the Fe center in addition to the direct excitation of Fe–O clusters (see Fig. 2).

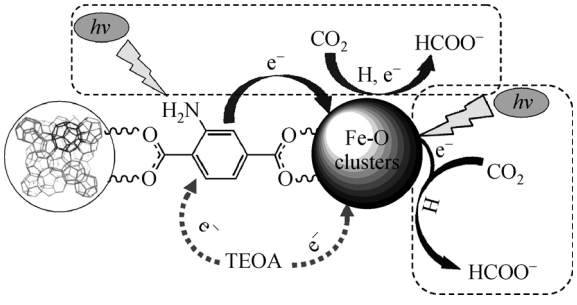

Fig. 2 Proposed CO_2 photoreduction through the dual excitation pathways over amino-functionalized Fe-based MOFs (Reproduced with permission from Ref. [95]. Copyright 2014, American Chemical Society)

2.2 Modification of organic linkers

Functionalization of organic linkers has been considered as an effective approach to increase the absorption of light and decrease the recombination rate of the photo-generated charge carriers and consequently to improve the photo-

catalytic reduction of CO_2. To date, several different organic linker functionalization strategies have been developed for enhancing the photocatalytic performance of MOFs toward CO_2 reduction under light illumination, including amine functionalization, utilization of porphyrin-based organic linkers, and photosensitizer functionalization.

2.2.1 Amine functionalization

Studies have shown that amine groups incorporated into the organic linkers in MOFs contribute to the CO_2 adsorption capacity enhancement, adsorption region broadening, and CO_2 photoreduction performance boost. The introduction of amine groups into aromatic polycarboxylates in MOFs can increase the interactions between CO_2 molecules and the modified linkers [119]. The CO_2 photoreduction improvement is attributed to the lone pair of electrons in amine groups, which can interact with the π*-orbitals of the benzene ring, leading to the donation of electrons to the anti-bonding orbitals. This interaction enables the formation of a new higher energy HOMO level, which leads to a broader optical absorption region and consequently enhanced CO_2 photoreduction [69].

In 2012, Li and coworkers [53], for the first time, prepared an amino-functionalized MOF, NH_2-MIL-125 (Ti), and examined CO_2 adsorption and photoreduction under visible light irradiation. NH_2-MIL-125(Ti) had a higher CO_2 adsorption capacity (132.2 cm^3/g) in comparison to that of MIL-125(Ti) (98.6 cm^3/g) due to the increased interaction between CO_2 molecules and the amine-modified linkers. Moreover, amine functionalization led to a broader adsorption range of 550 nm for NH_2-MIL-125(Ti) compared to MIL-125(Ti) with an adsorption range of 350 nm (see Fig. 3(a)). Photoreduction of CO_2 over NH_2-MIL-125(Ti) was performed in MeCN solvent with TEOA as an electron donor. After visible light irradiation for 10 h, 8.14 μmol of $HCOO^-$ was obtained, which was much higher than that of MIL-125(Ti) with no yield. The photocatalytic mechanism is proposed as follows (see Fig. 3(b)): under visible light irradiation, electrons are transferred from organic linkers to Ti^{4+} cations, and Ti^{4+} cations are reduced to Ti^{3+} by TEOA acting as an electron donor, leading to the formation of a long-lived excited charge separation. Ti^{3+} cations subsequently reduce CO_2 to $HCOO^-$. In 2013, the same research group (Li and coworkers) [93] developed another amino-functionalized MOF, NH_2-UiO-66(Zr), and found that it had a higher activity for CO_2 photoreduction than previously reported NH_2-MIL-125(Ti) in the presence of TEOA as a sacrificial agent. Similar to previous reports, substitution of the organic linker in UiO-66(Zr) by NH_2-BDC led to a broader optical absorption range of NH_2-UiO-66(Zr) due to the increased interaction between the NH_2-BDC linker and the Zr-O clusters. CO_2 uptake of NH_2-UiO-66(Zr) (68 cm^3/g) was also improved in comparison to the parent UiO-66(Zr) (53 cm^3/g) owing to the enhanced interactions of the NH_2 functional groups with the CO_2 molecules [119,120]. After visible light irradiation over NH_2-UiO-66(Zr) for 10 h, 13.2 μmol of $HCOO^-$ was produced. Partial substitution of the organic linker NH_2-BDC by $(NH_2)_2$-BDC in NH_2-UiO-66(Zr) further improved its CO_2 photoreduction activity, which gave 20.7 μmol of $HCOO^-$ under the same conditions as over NH_2-UiO-66(Zr) (Fig. 4). The improvement in CO_2 photocatalytic reduction over the mixed NH_2-UiO-66(Zr) is attributed to enhanced light absorption in the visible region and increased CO_2 adsorption (71 cm^3/g). Similar results were reported by Cohen and coworkers [94] who investigated the CO_2 photocatalytic reduction performance over $(NH_2)_2$-UiO-66(Zr) and $(NH_2)_2$-UiO-66(Zr/Ti) prepared by the introduction of diamine-substituted ligands into (NH_2)-UiO-66(Zr) and (NH_2)-UiO-66(Zr/Ti), respectively. It was found that an increase of the amino group

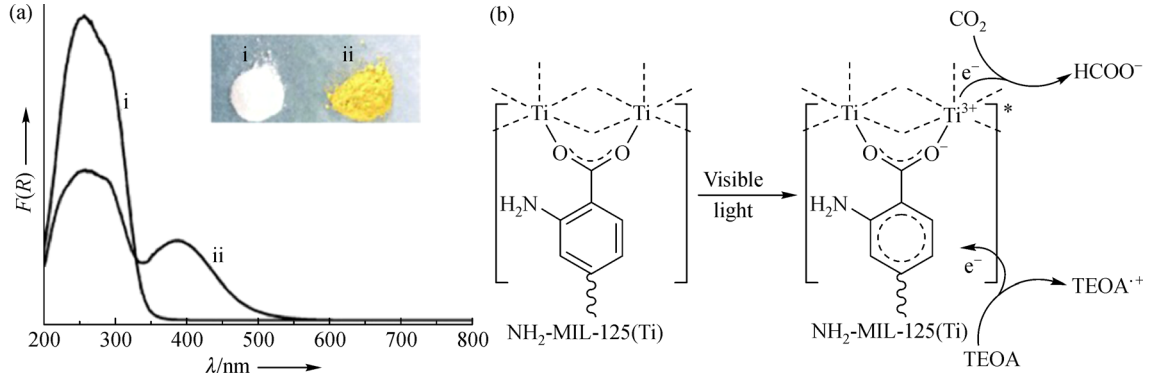

Fig. 3 Enhanced visible light absorption in NH_2-MIL-125(Ti) induced by amino functionality and the proposed CO_2 photoreduction mechanism

(a) UV-visible spectra of i) MIL-125(Ti) and ii) NH_2-MIL-125(Ti) (The inset shows the samples of i) MIL-125(Ti) and ii) NH_2-MIL-125(Ti).); (b) proposed CO_2 photoreduction mechanism over NH_2-MIL-125(Ti) under visible light irradiation (Reproduced with permission from Ref. [53].)

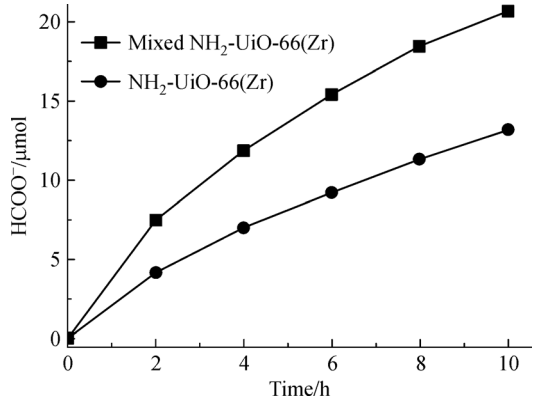

Fig. 4 Amount of $HCOO^-$ produced over NH_2-UiO-66(Zr) and mixed NH_2-UiO-66(Zr) as a function of light irradiation time (Reproduced with permission from Ref. [93]. Copyright 2013, Wiley)

number introduced new energy levels for additional light absorption and charge transfer, leading to enhancement in photocatalytic activities.

2.2.2 Utilization of porphyrin-based organic linkers

Porphyrins have complex cyclic structures consisting of four pyrrole rings linked to each other by methine groups. Due to their strong interactions with CO_2, high light adsorption efficiency and catalytic performance, porphyrin-based organic linkers have been incorporated into MOFs for CO_2 photoreduction.

Su and coworkers [97] prepared a rhodium(III)-porphyrin zirconium MOF (Rh-PMOF-1(Zr)) using a Rh-based metalloporphyrin tetracarboxylic ligand Rh (TCPP)Cl (TCPP = tetrakis(4-carboxyphenyl) porphyrin) and $ZrCl_4$. The CO_2 adsorption and photoreduction over Rh-PMOF-1(Zr) were examined. Rh-PMOF-1(Zr) had a high CO_2 adsorption capacity of 53 cm^3/g at 298 K. After visible-light irradiation for 18 h, the yield of $HCOO^-$ reached 6.1 $\mu mol/\mu mol_{cat}$. This showed that Rh-PMOF-1 (Zr) had a long-lived excited-state under vacuum at 298 K with the lifetime of 207 μs, which contributed to the improvement in the photocatalytic activity of Rh-PMOF-1 (Zr). Two catalytic reactions contribute to the CO_2 photocatalytic reduction to the formation of $HCOO^-$ over Rh-PMOF-1(Zr): ① metalloporphyrin ligand plays a role of an antenna to harvest light, generate electrons, and transfer electrons to the zirconium oxo clusters, reducing CO_2 to $HCOO^-$, and ② the rhodium-porphyrin ligands serve as photocatalytic centers toward CO_2 photoreduction.

Sharifnia and coworkers [98] used TCPP as ligand and $Zn(NO_3)_2 \cdot 6H_2O$ to prepare a porphyrin-based MOF (Zn/PMOF) and performed photocatalytic reduction of CO_2 over Zn/PMOF in the presence of H_2O vapor under UV-visible light. After 4 h irradiation, Zn/PMOF had a CO_2 photoreduction activity with CH_4 formation of 10.43 μmol. Only a small amount of CH_4 (10.77 μmol) was produced by extending the irradiation time to 24 h, which may have been caused by the fact that the intermediate product and/or byproduct formed after 4 h have saturated the active sites.

Huang et al. [99] synthesized two types of porphyrin-based MOFs, Al/PMOF and Cu-Al/PMOF, and compared their CO_2 adsorption capacities and photoreduction of CO_2 toward methanol. Al/PMOF was synthesized using TCPP as organic linker and $AlCl_3 \cdot 6H_2O$ while Cu-Al/PMOF was produced by doping Cu^{2+} into Al/PMOF. It showed that Cu^{2+} in Cu-Al/PMOF contributed to the enhanced photocatalytic reduction of CO_2. Cu-Al/PMOF had a higher CO_2 adsorption capacity (277.4 mg/g) than that of Al/PMOF (153.1 mg/g). Moreover, the methanol formation rate over Cu-Al/PMOF (262.6 ppm/(g·h)) was 7 times as high as that of Al/PMOF (37.5 ppm/(g·h)). As demonstrated by *in situ* Fourier transform infrared (FT-IR) spectra, CO_2 could be chemically adsorbed on the Cu site in Cu-Al/PMOF, where the linear CO_2 molecules would bend, thus lowering the reaction barrier and improving the photocatalytic efficiency.

Ye and coworkers [100] prepared MOF-525 ($Zr_6O_4(OH)_4$(TCPP-H_2)$_3$) by integrating Zr_6 clusters with porphyrin-based organic linkers. MOF-525-Co and MOF–525-Zn were also developed by the introduction of coordinatively unsaturated Co sites and Zn sites into the porphyrin units of MOF-525, respectively. As shown in Fig. 5, both MOF-525-Co (33.6 cm^3/g) and MOF-525-Zn (28.1 cm^3/g) had a higher CO_2 adsorption capacity than that of pristine MOF-525 (25.3 cm^3/g) due to the enhanced interaction between CO_2 molecules and the introduced open Co and Zn metal sites. CO_2 photoreduction over MOF-525, MOF-525-Co and MOF-525-Zn was performed in the presence of MeCN solvent and TEOA as an electron donor under visible light irradiation for 6 h, and two products, CO and CH_4 were produced. MOF-525-Co had the highest CO evolution rate of 200.6 μmol/(g·h) (yield: 2.42 μmol), and a CH_4 evolution rate of 36.76 μmol/(g·h) (yield: 0.42 μmol), followed by MOF-525-Zn (CO, 111.7 μmol/(g·h); CH_4, 11.635 μmol/(g·h)) and MOF-525 (CO, 64.02 μmol/(g·h); CH_4, 6.2 μmol/(g·h)). The photocatalytic activity enhancement for MOF-525-Co and MOF–525-Zn is partially ascribed to the difference in their charge separation efficiencies. MOF-525-Co and MOF-525-Zn had an enhanced efficiency in charge separation because of the lower energy at Co or Zn site, to which the electrons can be transferred from porphyrin units with a higher easiness. Furthermore, MOF-525-Co had a higher electron transfer efficiency (62.1 %) than that of MOF-525-Zn (24.9 %). These partially account for the better catalytic activity of MOF-525-Co than that of MOF-525-Zn. In addition, MOF-525-Co had a good stability and a good reproducible photocatalytic activity after three cycles (Fig. 5).

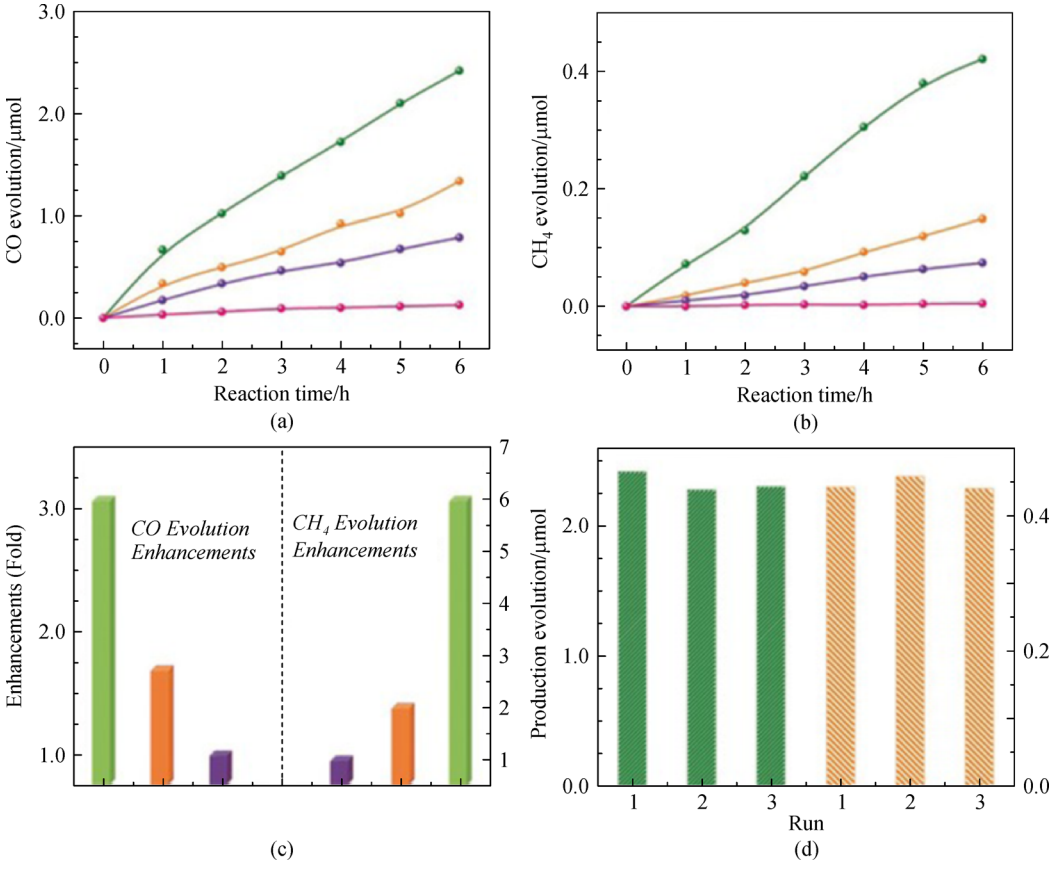

Fig. 5 Effect of metallization on the photocatalytic behavior of MOF-525

(a) Evolution rate of CO; (b) evolution rate of CH_4 over MOF-525-Co (green), MOF-525-Zn (orange), MOF-525 (purple) photocatalysts, and H_6TCPP ligand (pink) as a function of reaction time; (c) enhancement of production evolution over MOF-525-Co (green), MOF-525-Zn (orange), and MOF-525-Zn (purple); (d) production yield of CO (green) and CH_4 (orange) over MOF-525-Co photocatalyst as a function of cycling runs (Reproduced with permission from Ref. [100]. Copyright 2016, Wiley)

Xu et al. [101] prepared a zirconium-porphyrin MOF, PCN-222 (also named as MOF-545 or MMPF-6), by employing zirconium (IV) chloride and TCPP as ligand. PCN-222 had a CO_2 uptake of 35 cm^3/g at 298 K and 1 atm. Photocatalytic reduction of CO_2 over PCN-222 was performed in MeCN as solvent and TEOA as a sacrificial agent. After visible light irradiation for 10 h, $HCOO^-$ was produced with a yield of 30 μmol, which was much higher than that observed over the TCPP ligand alone (2.4 μmol), as shown in Fig. 6. It is proposed that upon irradiation, the TCPP in PCN-222 acts as an antenna to harvest visible light, generate electron–hole pairs, and transfer electrons to the Zr-oxo clusters toward CO_2 reduction to $HCOO^-$ in the presence of TEOA as the electron donor. Two factors contribute to the enhancement in photocatalytic performance of PCN-222: ① the high CO_2 adsorption capacity of PCN-222 might enable higher interaction with CO_2 in MeCN, thereby promoting the photocatalytic reaction, and ② the ultrafast transient absorption and photoluminescence spectroscopy reveals that the emergence of an extremely long-lived electron trap state in PCN-222 significantly suppresses the electron-hole recombination, thus enhancing the CO_2 photoreduction efficiency.

2.2.3 Photosensitizer functionalization

Photosensitizers are able to harvest light to generate electron-hole pairs and act as catalyst sites for CO_2 photoreduction. Photoactive metal complexes, such as Ru, Re, and Ir-based polypyridine units, have been widely used to functionalize MOFs to enhance their CO_2 photocatalytic reaction activities by introducing catalytic active centers and photosensitive sites for visible light harvesting [121–123].

Yan et al. [102] produced an Eu-Ru(phen)$_3$-MOF (phen = phenanthroline) by integrating the triangular Ru(phen)$_3$-derived tricarboxylate ligand as photosensitizer into Eu-MOF with Eu(III)$_2$(μ_2-H_2O) SBUs. Transient absorption results and theoretical calculations showed that photoexcitation of the Ru metalloligands in Eu-Ru(phen)$_3$-MOF initiated electron transfer into the nodes to generate dinuclear [Eu(II)]$_2$ active sites, which selectively converted CO_2 to $HCOO^-$ with a yield of 47 μmol in 10 h in the presence of MeCN and TEOA under visible light irradiation. This was higher than that observed over the Ru(phen)$_3$-derived tricarboxylate acid metalloligand alone under the same condition.

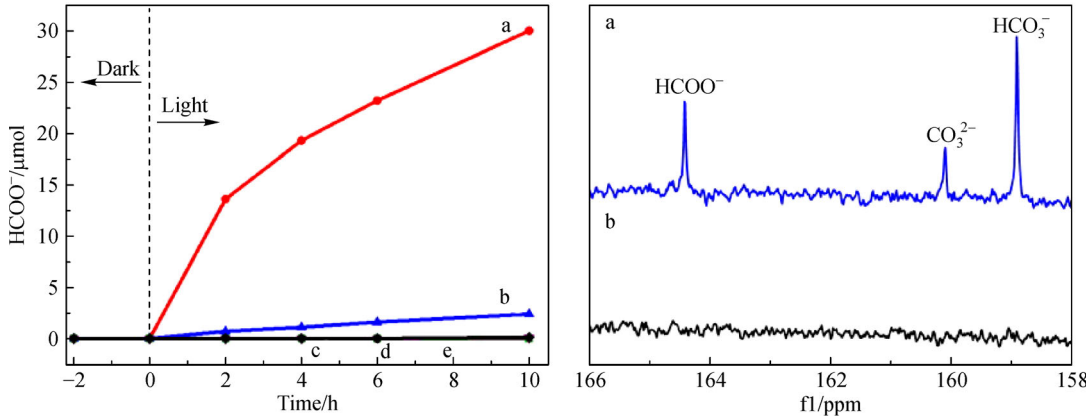

Fig. 6 Left: Amount of $HCOO^-$ produced as a function of visible light irradiation time over PCN-222 (a), H_2TCPP (b), no PCN-222 (c), no TEOA (d), and no CO_2 (e). Right: ^{13}C Nuclear magnetic resonance (NMR) spectra for the product obtained from reaction with $^{13}CO_2$ (a) or $^{12}CO_2$ (b) (Reproduced with permission from Ref. [101]. Copyright 2015, American Chemical Society)

Lin and coworkers [103] incorporated $Re^I(CO)_3$(5,5′-dcbpy)Cl (at 4 wt% doping level, 5,5′-dcbpy = 2,2'-bipyridine-5,5′-dicarboxylic acid) into the UiO-67 framework built from $Zr_6(\mu_3\text{-}O)_4(\mu_3\text{-}OH)_4$ SBUs and BPDC ligands, and tested the photocatalytic reduction of CO_2 in MeCN solvent and trimethylamine (TEA) as a sacrificial agent under visible light. The total turnover number (TON) of CO and H_2 over the as-doped UiO-67 reached 5.0 and 0.5, respectively, under visible light irradiation of 6 h. After 20 h, CO-TON and H_2-TON reached 10.9 and 2.5, respectively, which were higher than that observed for the bare $Re^I(CO)_3$(5,5′-dcbpy)Cl (CO-TON = 7.0, H_2-TON = 1.0) under the same condition because of the decomposition of $Re^I(CO)_3$(5,5′-dcbpy)Cl under irradiation. This enhanced TON is proposed to be associated with the stabilization effect of the active-site isolation of the immobilized Re-based catalysts in the framework. Lately, the same group produced another photosensitizer-functionalized MOF, $Zr_6(O)_4(OH)_4[Re(CO)_3Cl(bpydb)]_6$(MOF-**1**), by integrating the elongated linear (bpy)Re$(CO)_3Cl$-containing dicarboxylate ligand (bpydb = 4,4'-(2,2'-bipyridine-5,5′-diyl)dibenzoate; bpy = 2,2'-bipyridine) with $Zr_6(\mu_3\text{-}O)_4(\mu_3\text{-}OH)_4$ SBUs (Fig. 7) [104]. Under the same experimental condition as described above, CO-TON and H_2-TON reached 6.44 and 0.4 in 6 h, respectively, which were higher than those of the homogeneous counterpart (CO-TON = 1.12 and H_2-TON 0.18). Ryu et al. [52] embedded $Re^I(CO)_3$(5,5′-dcbpy)Cl and amine (-NH_2) functional group within UiO-67 (denoted as Re-MOF-NH_2) and varied the ratio of the-NH_2 functional groups from 0 to 80 mol%. Photocatalytic CO_2 conversion was performed in the presence of TEA under visible light. The results showed that Re-MOF-NH_2 incorporated with 33 mol% of -NH_2 functional groups had the highest photocatalytic CO_2 conversion rate (1.5 μmol/(g·h)) to CO, which was three times as that observed for Re-MOF without -NH_2 incorporation (0.5 μmol/(g·h)). The enhancement in photocatalytic activity is caused by the induced different bond lengths for Re-CO in $Re^I(CO)_3$(5,5′-dcbpy)Cl by the incorporation of -NH_2 functional groups, which endows the intermolecular stabilization of carbamate with CO_2, thus boosting the photocatalytic activity. Fontecave and coworkers [105] functionalized UiO-67 MOF by replacing 5%–35% of BPDC linkers with Cp*Rh(5,5′-bpydb)Cl_2 (Cp* = pentamethylcyclopentadiene) (named as Cp*Rh@UiO-67). Under visible light irradiation for 10 h in the presence of acetonitrile (ACN) and TEOA, $HCOO^-$-TON and H_2-TON of 10%-Cp*Rh@UiO-67 reached 47 and 36, respectively, with $[Ru(bpy)_3]Cl_2$ as a photosensitizer.

Li and coworkers [106] incorporated $Ru(CO)_2Cl_2$ into MOF-253 (Al(OH)(5,5′-dcbpy)), named as MOF-253-Ru$(CO)_2Cl_2$, and enhanced the CO_2 photoreduction by producing 0.67 μmol of $HCOO^-$, 1.86 μmol of CO as well as 0.09 μmol H_2 after irradiation under visible light for 8 h in MeCN and TEOA, whereas no products were detected over pristine MOF-253 under the same condition. The performance of MOF-253-Ru$(CO)_2Cl_2$ was further improved via photosensitizer ($Ru(bpy)_2Cl_2$) functionalization, by enhancing the light absorption in the visible light region. The $HCOO^-$, CO, and H_2 produced in 8 h over sensitized MOF-253-Ru$(CO)_2Cl_2$ ($Ru(bpy)_2Cl_2$/Ru-complex was 1: 2) was 4.84, 1.85, and 0.72 μmol, respectively, which was much higher than those observed over the non-sensitized MOF-253-Ru$(CO)_2Cl_2$ under the same condition. In the sensitized MOF-253-Ru$(CO)_2Cl_2$, Ru$(CO)_2Cl_2$ reacted with the surface *N,N*-chelated sites to form MOF-253-supported $Ru(bpy)_2(X_2bpy)^{2+}$, which extended the light absorption edge to 630 nm, wider than that of MOF-253-Ru$(CO)_2Cl_2$ (470 nm), thus promoting the photocatalytic CO_2 reduction. However, a decrease in the photoreactivity of the sensitized MOF-253-Ru$(CO)_2Cl_2$ was observed with increasing the amount of the photosensitizer $Ru(bpy)_2Cl_2$, which might be attributed to the pore

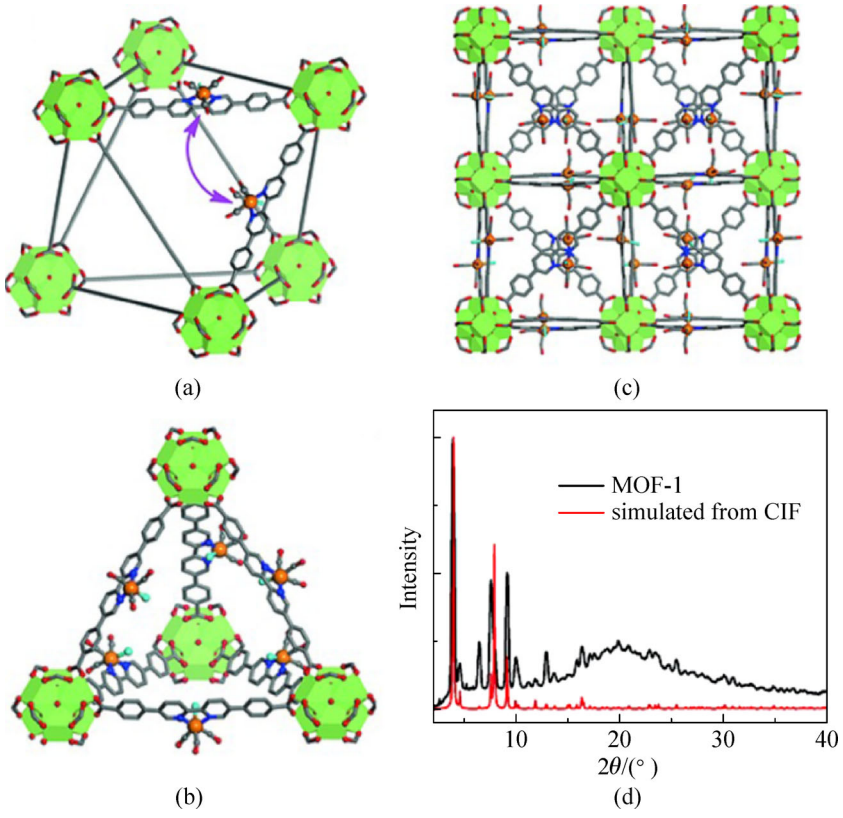

Fig. 7 Crystal structure of $Zr_6(O)_4(OH)_4[Re(CO)_3Cl(bpydb)]_6$ (MOF-**1**)
(a) Showing an octahedral cage; (b) showing a tetrahedral cage with SBUs displayed as polygons; (c) as viewed along the [100] direction of the unit cell; (d) X-ray diffraction(XRD) (black) and simulated XRD pattern (red) of MOF-**1** (Reproduced with permission from Ref. [104]. Copyright 2016, Wiley)

blocking of MOF-253 by the $Ru(bpy)_2Cl_2$.

Luo and coworkers [107] developed a photocatalytic MOF ($Y[Ir(ppy)_2(4,4'\text{-dcbpy})]_2[OH]$) (Ir-CP, ppy: 2-phenylpyridine, 4,4'-dcbpy: 2,2'-bipyridine-4,4'-dicarboxylate) using $Y(NO_3)_3$ and $Ir(ppy)_2(Hdcbpy)$. Photoreduction of CO_2 over Ir-CP was performed in MeCN and TEOA under visible light irradiation. It showed that 38.0 μmol $HCOO^-$ was produced in 6 h, with a product formation rate of 118.8 μmol /(g·h). The photocatalytic mechanism is proposed as follows: the $[Ir(ppy)_2(dcbpy)]^-$ unit in Ir-CP is excited under visible light and is reductively quenched by TEOA, and the CO_2 molecules are reduced to $HCOO^-$ by getting electrons from $[Ir(ppy)_2(dcbpy)]^{2-}$ units. Lately, the same group [108,109] incorporated Ru-polypyridine complexes into MOF structures as metalloligands and produced a series of photocatalytic MOFs. Ru-MOF, with a chemical formula of $[Cd_2[Ru(4,4'\text{-dcbpy})_3]\cdot 12H_2O]_n$, was constructed from $[Cd_2(CO_2)_6]$ SBUs and $[Ru(4,4'\text{-dcbpy})_3]^{4-}$ metalloligands [108]. The morphologies of Ru-MOF can be tuned to form nanoflowers, microflakes, and bulk crystals structures by controlling the reactants concentration, as shown in Fig. 8. In the mixture of MeCN/TEOA, Ru-MOF nanoflowers had the highest $HCOO^-$ formation rate of 77.2 μmol/(g·h) under visible light irradiation for 8 h, followed by microflakes (52.7 μmol/(g·h)) and bulk crystals (30.6 μmol/(g·h)). The Ru-MOF nanoflowers had a better photocatalytic activity than their bulk counterparts because of their high visible light harvesting and long-lasting excited-state originated from their large surface area (8.08 m^2/g; microflake: 1.33 m^2/g) and high energy transfer efficiency. After this work, Luo and coworkers [109] synthesized two Ru-polypyridine-functionalized MOFs, $[Cd_3[Ru(5,5'\text{-dcbpy})_3]_2\cdot 2(Me_2NH_2)]_n$ and $[Cd[Ru(bpy)(4,4'\text{-dcbpy})_2]\cdot 3H_2O]_n$, with non-interpenetrated and interpenetrated structures, respectively. CO_2 photoreduction over the two MOFs was conducted in the presence of MeCN and TEOA under visible light irradiation. It showed that the $HCOO^-$ production over $[Cd_3[Ru(5,5'\text{-dcbpy})_3]_2\cdot 2(Me_2NH_2)]_n$ and $[Cd[Ru(bpy)(4,4'\text{-dcbpy})_2]\cdot 3H_2O]_n$ reached 16.1 and 17.2 μmol in 6 h (with a production rate of 67.5 and 71.7 μmol/(g·h)), respectively. The difference in photocatalytic performance of the two MOFs may have been associated with their structural stabilities. $[Cd_3[Ru(5,5'udcbpy)_3]_2\cdot 2(Me_2NH_2)]_n$ has a non-interpenetrated structure in which the porous framework is supported by the coordination between metal ions and organic linkers as well as the interactions between the framework and the guest molecules in the pores. In the photocatalytic process, the exchange of guest molecules

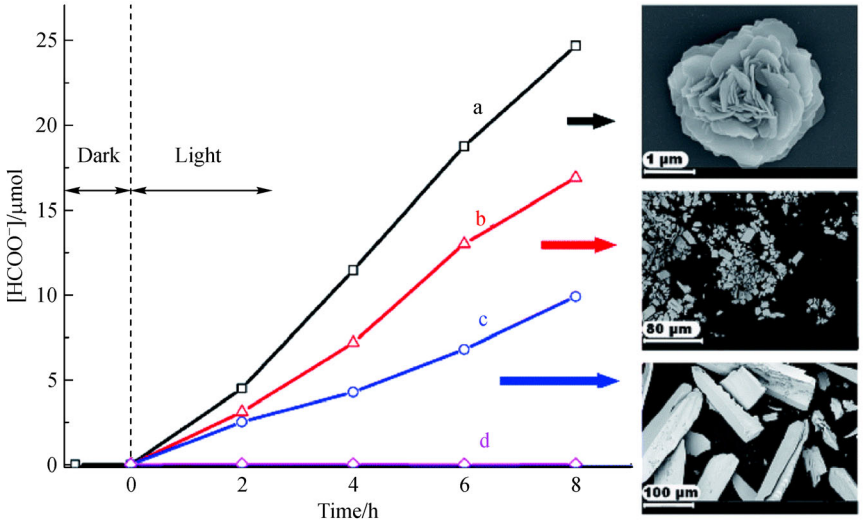

Fig. 8 Amount of $HCOO^-$ produced as a function of irradiation time of visible light over (a) nanoflowers, (b) microcrystals, and (c) bulk crystals of the Ru-MOF ($[Cd_2[Ru(4,4'\text{-dcbpy})_3]\cdot 12H_2O]_n$). (d) visible light irradiation without a sample (Inset images (from top to bottom) show nanoflowers, microcrystals and bulk crystals of the Ru-MOF, respectively. Reproduced with permission from Ref. [108]. Copyright 2015, Royal Society of Chemistry)

with the solvent molecules may cause the collapse of structure, leading to the decrease in photocatalytic activity. In contrast, $[Cd[Ru(bpy)(4,4'\text{-dcbpy})_2]\cdot 3H_2O]_n$ with an interpenetrated structure has a higher structural stability, which endows its better photocatalytic activity than $[Cd_3[Ru(5,5'\text{-dcbpy})_3]_2\cdot 2(Me_2NH_2)]_n$.

In addition to the ligand functionalization strategies discussed as above, catechol- [110] and anthracene-based [111] organic linkers were also utilized to functionalize MOF structures, which all had high photocatalytic performances on CO_2 reduction.

3 MOF composite photocatalysts

MOFs have shown much potential on CO_2 photoreduction thanks to their large surface areas, high CO_2 uptake, as well as tunable structures and optical properties. To further improve the photocatalytic performance of MOFs, photosensitizers, semiconductors, metals and carbon materials have been incorporated into MOF structures to promote photo-generated electrons transfer and charge separation processes. The performances of MOF composites as photocatalysts for CO_2 reduction are summarized in Table 3.

3.1 MOF composites incorporated with photosensitizers

As discussed in Section 2.2.3, metal-complex photosensitizers have been used to functionalize MOFs to enhance the photocatalytic activity. Photosensitizers can also be incorporated into MOFs to produce MOF composites for CO_2 photoreduction.

Ru-based photosensitizer has been incorporated into several MOFs to enhance CO_2 photocatalytic reduction [57–59]. Wang and coworkers [57] investigated the performance of a series of MOFs (Co-ZIF-9, Co-MOF-74, Mn-MOF-74, Zn-ZIF-8, Zr-UiO-66-NH_2) in conjunction with $[Ru(bpy)_3]Cl_2\cdot 6H_2O$ toward CO_2 photocatalytic reduction, where the MOF acts as a co-catalyst and $[Ru(bpy)_3]Cl_2\cdot 6H_2O$ acts as a photosensitizer. Photoreduction of CO_2 was performed in MeCN and H_2O solvent with TEOA as a sacrificial agent. After visible light irradiation for 0.5 h, 41.8 μmol of CO and 29.9 μmol of H_2 were obtained over Co-ZIF-9 incorporated with $[Ru(bpy)_3]Cl_2\cdot 6H_2O$, which outperformed the counterparts with a lower yield of CO and H_2 under the same condition (as shown in Table 3). Co-ZIF-9 is a microporous cobalt-containing benzimidazolate MOF. The superior performance of Co-ZIF-9 with regard to CO_2 photocatalytic reduction is a result of the synergetic effect of the imidazolate-based ligand which has a strong interaction with CO_2 molecules for CO_2 adsorption and cobalt with electron-mediating functions. Lately, the same group incorporated $[Ru(bpy)_3]Cl_2\cdot 6H_2O$ as a photosensitizer into Co-ZIF-67 acting as a co-catalyst [59]. Under the similar reaction condition, 37 μmol of CO and 13 μmol of H_2 were produced over Co-ZIF-67/$[Ru(bpy)_3]Cl_2\cdot 6H_2O$ in 0.5 h under visible light irradiation. This was higher than that observed over Zn-ZIF-8/$[Ru(bpy)_3]Cl_2\cdot 6H_2O$ (1.8 μmol of CO and 2.0 μmol of H_2 production in 0.5 h under the same condition), where the co-catalyst Zn-ZIF-8 has the same organic linker (2-methylimidazole) as Co-ZIF-67 but different metal site (Zn-based). This further confirmed the effect of cobalt on the photocatalytic reaction.

Cohen and coworkers [58] incorporated a photosensiti-

Table 3 Performances of recent photocatalytic MOF composites for CO_2photoreduction

Strategy	MOF composite	Irradiation	Solvent/ sacrificial agent	Main product	Photocatalytic reactivity	Reaction time/h	Ref.
Photosensitizer incorporation	Co-ZIF-9/$[Ru(bpy)_3]Cl_2\cdot 6H_2O$	Visible	MeCN/H_2O/ TEOA	CO	41.8 μmol	0.5	[57]
				H_2	29.9 μmol		
	Co-MOF-74/$[Ru(bpy)_3]Cl_2\cdot 6H_2O$			CO	11.7 μmol		
				H_2	7.3 μmol		
	Mn-MOF-74/$[Ru(bpy)_3]Cl_2\cdot 6H_2O$			CO	1.5 μmol		
				H_2	2.9 μmol		
	Zn-ZIF-8/$[Ru(bpy)_3]Cl_2\cdot 6H_2O$			CO	2.1 μmol		
				H_2	2.4 μmol		
	Zr-UiO-66-NH_2/$[Ru(bpy)_3]Cl_2\cdot 6H_2O$			CO	1.2 μmol		
				H_2	2.2 μmol		
	Co-ZIF-67 /$[Ru(bpy)_3]Cl_2\cdot 6H_2O$	Visible	MeCN/H_2O/TEOA	CO	29.6 μmol	0.5	[59]
				H_2	14.8 μmol		
	Zn-ZIF-9/$[Ru(bpy)_3]Cl_2\cdot 6H_2O$			CO	1.8 μmol		
				H_2	2.0 μmol		
	Cu-HKUST-1/$[Ru(bpy)_3]Cl_2\cdot 6H_2O$			CO	1.2 μmol		
				H_2	1.5 μmol		
	Fe-MIL-101-NH_2/$[Ru(bpy)_3]Cl_2\cdot 6H_2O$			CO	4.7 μmol		
				H_2	2.1 μmol		
	Zr-UiO-66-NH_2/$[Ru(bpy)_3]Cl_2\cdot 6H_2O$			CO	0.9 μmol		
				H_2	1.2 μmol		
	UiO-67-Mn(5,5′ - dcbpy) $(CO)_3Br$)/$Ru(dmb)_3(PF_6)_2$	Visible	DMF/TEOA/ BNAH	$HCOO^-$	TON = 50	4	[58]
					TON = 110	18	
	UiO-67-Mn(5,5′ - dcbpy)$(CO)_3Br$) (without a photosensitizer)				TON = 18	18	
	Mn(5,5′ - dcbpy)$(CO)_3Br$)/ $Ru(dmb)_3(PF_6)_2$				TON = 32	4	
					TON = 57	18	

(*Continued*)

Strategy	MOF composite	Irradiation	Solvent/ sacrificial agent	Main product	Photocatalytic reactivity	Reaction time/h	Ref.
	$Mn(bpy)(CO)_3Br)/Ru(dmb)_3(PF_6)_2$				TON = 35	4	
					TON = 70	18	
	UiO-67-5,5′ - dcbpy)/$Ru(dmb)_3(PF_6)_2$				TON = 38	18	
	$[Ru(dmb)_3]^{2+}$			$HCOO^-$	TON = 33	18	
Semiconductor incorporation	ZIF-8/TiO_2 (ZIF-8 growth step on TiO_2 film was repeated twice)	UV	H_2O vapor	CO	0.53 μmol/(g·h)	5	[124]
				CH_4	0.18 μmol/(g·h)		
	ZIF-8/Ti/TiO_2 nanotube	UV-visible	Na_2SO_4 (0.1 mol/L)	C_2H_5OH	10 mmol/L	3	[125]
				CH_3OH	0.7 mmol/L		
	Co-ZIF-9/TiO_2 (mass ratio of Co-ZIF-9 in composite is 0.03)	UV-visible	H_2O vapor	CO	8.79 μmol	10	[54]
				CH_4	0.99 μmol		
				H_2	1.30 μmol		
	TiO_2			CO	3.58 μmol		
				CH_4	0.60 μmol		
				H_2	0.63 μmol		
	Co-ZIF-9			CO	0		
				CH_4	0		
				H_2	0		
	Physical mixture of TiO_2 and Co-ZIF-9 with the mass ratio of 0.03:0.97			CO	3.86 μmol		
				CH_4	0.42 μmol		
				H_2	0.56 μmol		
	Cu-BTC/TiO_2	UV	H_2O vapor	CH_4	2.64 μmol/(g_{TiO_2}·h)	4	[126]
	TiO_2			CH_4	0.52 μmol/(g_{TiO_2}·h)		
				H_2	2.29 μmol/(g_{TiO_2}·h)		
	Cu-BTC			CH_4	0		
				H_2	0		
	Cu-BTC/TiO_2 (molar ratio of Cu-BTC to TiO_2 is 3.33)	N/A	CO_2/H_2O vapor	CO	256.38 μmol/(g_{TiO_2}·h)	8	[127]

(*Continued*)

Strategy	MOF composite	Irradiation	Solvent/ sacrificial agent	Main product	Photocatalytic reactivity	Reaction time/h	Ref.
	TiO_2				11.48 μmol/(g_{TiO2}·h)		
	Cu-BTC				0		
	CPO-27-Mg/TiO_2	UV	H_2O vapor	CO	40.9 μmol/g	10	[128]
				CH_4	23.5 μmol/g		
	TiO_2			CO	22.5 μmol/g		
				CH_4	13.7 μmol/g		
	CPO-27-Mg			CO	0		
				CH_4	0		
	Physical mixture of TiO_2 and CPO-27-Mg with the ratio of 6:4			H_2	8.5 μmol/g		
				CO	18.9 μmol/g		
				CH_4	7.1 μmol/g		
	NH_2-UiO-66/TiO_2 (with 19%(wt) NH_2-UiO-66)	UV-visible	CO_2/H_2	CO	3.74 μmol/(g·h)		[129]
	NH_2-UiO-66/TiO_2 (19.5%(wt)NH_2-UiO-66)				4.24 μmol/(g·h)		
	NH_2-UiO-66/TiO_2 (24.5%(wt) NH_2-UiO-66)				3.37 μmol/(g·h)		
	NH_2-UiO-66/TiO_2 (36.8%(wt) NH_2-UiO-66)				2.85 μmol/(g·h)		
	TiO_2				2.85 μmol/(g·h)		
	NH_2-UiO-66				1.50 μmol/(g·h)		
	Co-ZIF-9/CdS	Visible	MeCN/H_2O /TEOA/bpy	CO	50.4 μmol	15	[130]
				H_2	11.1 μmol		
	Co-MOF-74/CdS			CO	39.6 μmol		
				H_2	7.7 μmol		
	Mn-MOF-74/CdS			CO	1.0 μmol		
				H_2	2.0 μmol		
	Zn-ZIF-8/CdS			CO	0.6 μmol		
				H_2	0.6 μmol		
	Zr-UiO-66-NH_2/CdS			CO	0.4 μmol		
				H_2	0.3 μmol		

(*Continued*)

Strategy	MOF composite	Irradiation	Solvent/ sacrificial agent	Main product	Photocatalytic reactivity	Reaction time/h	Ref.
	CdS			CO	0.5 μmol		
				H_2	0.6 μmol		
	Co-ZIF-9			CO	0		
				H_2	0		
	UiO-66-NH_2/$Cd_{0.2}Zn_{0.8}S$ (10%(wt)UiO-66-NH_2)	Visible	Na_2S/Na_2SO_3	H_2	4591.6 μmol/(g·h)		[55]
				CH_3OH	4.1 μmol/(g·h)		
	UiO-66-NH_2/$Cd_{0.2}Zn_{0.8}S$ (20%(wt)UiO-66-NH_2)			H_2	5846.5 μmol/(g·h)		
				CH_3OH	6.8 μmol/(g·h)		
	UiO-66-NH_2/$Cd_{0.2}Zn_{0.8}S$ (30%(wt)UiO-66-NH_2)			H_2	5235.9 μmol/(g·h)		
				CH_3OH	5.9 μmol/(g·h)		
	UiO-66-NH_2/$Cd_{0.2}Zn_{0.8}S$ (40%(wt)UiO-66-NH_2)			H_2	4922.7 μmol/(g·h)		
				CH_3OH	5.3 μmol/(g·h)		
	$Cd_{0.2}Zn_{0.8}S$			H_2	2804.2 μmol/(g·h)		
				CH_3OH	2.0 μmol/(g·h)		
	UiO-66-NH_2			H_2	0		
				CH_3OH	0		
	Co-ZIF-9/mesoporous g-C_3N_4	Visible	MeCN/H_2O /TEOA/bpy	CO	20.8 μmol	2	[131]
				H_2	3.3 μmol		
	Co-ZIF-9			CO	0		
				H_2	0		
	g-C_3N_4			CO	0		
				H_2	0		
	ZIF-8/g-C_3N_4 nanotubes (molar ratio of g-C_3N_4 nanotubes to ZIF-8 is 10)	UV-visible	CO_2/H_2O vapor	CH_3OH	0.64 μmol/(g·h)	1	[56]
	ZIF-8/g-C_3N_4 nanotubes (molar ratio of g-C_3N_4 nanotubes to ZIF-8 is 8)				0.75 μmol/(g·h)		
	ZIF-8/g-C_3N_4 nanotubes (molar ratio of g-C_3N_4 nanotubes to ZIF-8 is 5)				0.45 μmol/(g·h)		
	ZIF-8/g-C_3N_4 nanotubes (molar ratio of g-C_3N_4 nanotubes to ZIF-8 is 2)				0.31 μmol/(g·h)		

(*Continued*)

Strategy	MOF composite	Irradiation	Solvent/ sacrificial agent	Main product	Photocatalytic reactivity	Reaction time/h	Ref.
	ZIF-8/g-C_3N_4 nanotubes (molar ratio of g-C_3N_4 nanotubes to ZIF-8 is 1)				0.16 μmol/(g·h)		
	g-C_3N_4 nanotubes				0.49 μmol/(g·h)		
	Bulk g-C_3N_4				0.24 μmol/(g·h)		
	ZIF-8 nanocrystals				0		
	UiO-66/g-C_3N_4 nanosheets	Visible	MeCN/TEOA	CO	9.9 μmol/($g_{g\text{-}C_3N_4}$·h)	6	[132]
	UiO-66/bulk g-C_3N_4				3.2 μmol/($g_{g\text{-}C_3N_4}$·h)		
	g-C_3N_4 nanosheets				2.9 μmol/($g_{g\text{-}C_3N_4}$·h)		
	Bulk g-C_3N_4				2.0 μmol/($g_{g\text{-}C_3N_4}$·h)		
	UiO-66				0		
	BIF-20/g-C_3N_4 nanosheets (10%(wt) g-C_3N_4 nanosheets)	Visible	MeCN/TEOA	CO	3.42 μmol	6	[133]
				CH_4	1.12 μmol		
	BIF-20/g-C_3N_4 nanosheets (15%(wt) g-C_3N_4 nanosheets)			CO	4.86 μmol		
				CH_4	1.45 μmol		
	BIF-20/g-C_3N_4 nanosheets (20%(wt) g-C_3N_4 nanosheets)			CO	6.12 μmol		
				CH_4	1.76 μmol		
	BIF-20/g-C_3N_4 nanosheets (25%(wt) g-C_3N_4 nanosheets)			CO	5.14 μmol		
				CH_4	1.51 μmol		
	ZIF-8/Zn_2GeO_4 (25%(wt) ZIF-8)	N/A	Na_2SO_3	CH_3OH	0.22 μmol/(g·h)	11	[134]
Metal incorporation	Pt/NH_2-MIL-125(Ti)	Visible	MeCN/TEOA	$HCOO^-$	12.96 μmol	8	[135]
				H_2	235 μmol		
	Au/NH_2-MIL-125(Ti)			$HCOO^-$	9.06 μmol		
				H_2	40.2 μmol		
	NH_2-MIL-125(Ti)			$HCOO^-$	10.75 μmol		
				H_2	0		
	1%(wt) Co/NH_2-MIL-125(Ti)	Visible	MeCN/TEOA	$HCOO^-$	384.2 μmol	10	[136]
	2%(wt) Co/NH_2-MIL-125(Ti)				321.8 μmol		
	3%(wt) Co/NH_2-MIL-125(Ti)				239.4 μmol		
	NH_2-MIL-125(Ti)				162.8 μmol		
	Ag⊂Re_3-MOF (16 nm thick Re_3-MOF)	Visible	MeCN/TEOA	CO	TON ≈ 2.8	48	[137]

(*Continued*)

Strategy	MOF composite	Irradiation	Solvent/ sacrificial agent	Main product	Photocatalytic reactivity	Reaction time/h	Ref.
	$Re^{I}(CO)_3(5,5'$ - dcbpy)Cl				TON ≈ 1.7		
Carbon materials incorporation	1%(wt) UiO-66-NH_2/graphene	Visible	DMF/TEOA/H_2O	$HCOO^-$	12.3 μmol	4	[138]
				CH_4	0.25 μmol		
				H_2	15.2 μmol		
	1.5%(wt) UiO-66-NH_2/graphene			$HCOO^-$	21.2 μmol		
				CH_4	0.59 μmol		
				H_2	13.9 μmol		
	2%(wt) UiO-66-NH_2/graphene			$HCOO^-$	33.5 μmol		
				CH_4	0.90 μmol		
				H_2	13.2 μmol		
	2.5%(wt) UiO-66-NH_2/graphene			$HCOO^-$	14.9 μmol		
				CH_4	0.51 μmol		
				H_2	15.1 μmol		
	3%(wt) UiO-66-NH_2/graphene			$HCOO^-$	8.6 μmol		
				CH_4	0.19 μmol		
				H_2	16.8 μmol		
	UiO-66-NH_2			$HCOO^-$	3.1 μmol		
				CH_4	0.11 μmol		
				H_2	16.9 μmol		
	Graphene			$HCOO^-$	0		
				CH_4	0		
				H_2	0		
	UiO-66-NH_2/graphene (hydrothermal synthesis)			$HCOO^-$	16.1 μmol		
				H_2	20.4 μmol		
	Al-PMOF/5%(wt) NH_2-rGO	Visible	MeCN/TEOA	$HCOO^-$	685.6 μmol/(g·h)	6	[139]
	Al-PMOF/15%(wt) NH_2-rGO				479.8 μmol/(g·h)		
	Al-PMOF/25%(wt) NH_2-rGO				476.4 μmol/(g·h)		
	Al-PMOF				165.3 μmol/(g·h)		

Notes: CAN–acetonitrile; BNAH–1-benzyl-1,4-dihydronicotinamide; bpy–2,2'-bipyridine; BTC–benzene-1,3,5-tricarboxylate; Cp*–pentamethylcyclopentadiene; DMF–*N, N*-dimethylformamide; MeCN–acetonitrile; phen–phenanthroline; TEA–trimethylamine; TEOA–triethanolamine; TON–total turnover number; 5,5′-dcbpy–2,2'-bipyridine-5,5′-dicarboxylic acid; bpydb –4,4'-(2,2'-bipyridine-5,5′-diyl)dibenzoate; ppy–2-phenylpyridine; 4,4′-dcbpy–2,2'-bipyridine-4,4'-dicarboxylate; dmb–4,4′-dimethyl-2,2′-bipyridine

zer $[Ru(dmb)_3]^{2+}$ (dmb = 4,4′-dimethyl-2,2′-bipyridine) into UiO-67 which was functionalized with a Mn^+ bipyridine complex, Mn(5,5′-5,5′-dcbpy)-$(CO)_3Br$ for CO_2 photocatalytic reduction. In the mixture of *N, N*-dimethylformamide (DMF), TEOA and BNAH, $HCOO^-$ was produced with the TON of 110 under visible light irradiation for 18 h, which outperformed the UiO-67-Mn (5,5′-dcbpy)-$(CO)_3Br$ without a photosensitizer $[Ru(dmb)_3]^{2+}$ and the homogeneous reference systems (Fig. 9). The superior photocatalytic performance is attributed to the isolated active sites in MOF framework, which endows the high stability of the catalyst and impedes the dimerization of the singly reduced Mn complex.

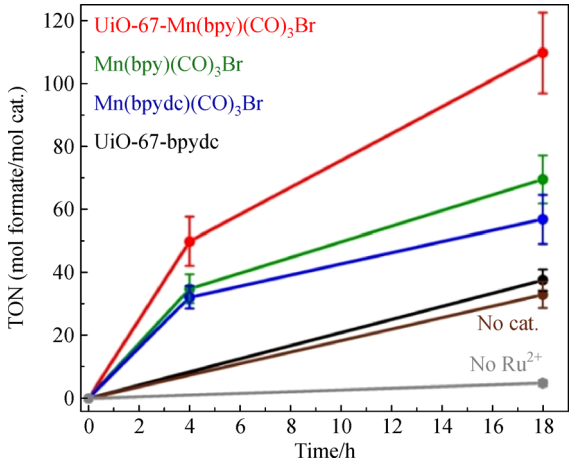

Fig. 9 TON of $HCOO^-$ as a function of reaction time over UiO-67-Mn(bpy)$(CO)_3Br$ (red), Mn(bpy)$(CO)_3Br$ (green), Mn(bpydc)$(CO)_3Br$ (blue), UiO-67-bpydc (black), no added Mn complex or MOF (only Ru^{2+}, brown), and UiO-67-Mn(bpy)$(CO)_3Br$ without added Ru^{2+} (gray) (Reproduced with permission from Ref. [58]. Copyright 2015, American Chemical Society)

3.2 MOF composites incorporated with semiconductors

Coupling MOFs with semiconductors has been shown to be another approach to reducing the recombination rate of the photo-generated charge carries and consequently enhancing the photocatalytic performance. Several types of semiconductors such as TiO_2, CdS and graphitic C_3N_4 have been embedded into MOFs to form heterogeneous structures which retain the properties of both the semiconductors and MOFs that are beneficial to CO_2 photocatalytic reactions.

3.2.1 MOF-TiO_2 composites

Several studies reported the development of ZIF-8/TiO_2 composites for CO_2 photoreduction. Zhang and coworkers [124] integrated ZIF-8 into the TiO_2 film grid and conducted CO_2 photocatalytic reactions in H_2O as an electron donor without the use of a sacrificial agent under UV irradiation for 5 h. The amount of ZIF-8 in ZIF-8/TiO_2 composite was varied by repeating the ZIF-8 growth step on the TiO_2 film from one to three times, which are denoted as TiMOF-1, TiMOF-2, and TiMOF-3, respectively. TiMOF-3 with the highest amount of ZIF-8 had the highest CO_2 adsorption uptake, followed by TiMOF-2, TiMOF-1, and TiO_2. TiMOF-2 had the best performance with a CO yield of 0.53 μmol/(g·h) and a CH_4 yield of 0.18 μmol/(g·h), which was 38% and 157% higher than that observed over pure TiO_2 film under the same condition. TiMOF-2 outperformed TiMOF-3 which had the highest CO_2 adsorption capacity due to the fact that the large amount of ZIF-8 in TiMOF-3 covered the TiO_2 film, impeding the photo excitation process of TiO_2. It is proposed that both TiO_2 and ZIF-8 can be activated to generate photo-induced charge carries under UV irradiation, while TiO_2 is more effective in the photoexcitation process than ZIF-8 because of its higher photoactivity and narrower band gap (–0.45 eV vs. –0.5 eV for ZIF-8). Electrons can also transfer from TiO_2 to ZIF-8 and be involved in the photoreduction process over ZIF-8.

Cardoso and coworkers [125] developed a MOF-based Ti/TiO_2 composite photocatalyst by growing ZIF-8 thin films on Ti/TiO_2 nanotube (NT) electrodes using a layer-by-layer process. Spectroscopic and voltammetric assays revealed that the CO_2 adsorbed on ZIF-8 formed stable carbamates. The photoelectrocatalytic reduction of CO_2 over Ti/TiO_2NT-ZIF-8 electrodes was performed in Na_2SO_4 (pH 4.5) saturated with CO_2 at a constant potential of + 0.1 V under UV-visible light irradiation. 10 mmol/L of ethanol and 0.7 mmol/L of methanol were produced in 3 h, which increased around 20 and 430 times, respectively, compared to the values observed over Ti/TiO_2NT due to the low CO_2 adsorption capacity of Ti^{4+} species in the absence of ZIF-8.

Co-ZIF-9/TiO_2 composites with different mass ratios of Co-ZIF-9 (named as ZIF_x/T; where x represents the mass ratios of Co-ZIF-9 in the composite, which equals 0.01, 0.03, 0.10, 0.20, 0.30, 0.40, and 0.60) were synthesized via an *in situ* synthetic method by Ye and coworkers for CO_2 photoreduction [54]. Of the ZIF_x/T composites, $ZIF_{0.03}$/T had the best photocatalytic performance with a CO yield of 8.79 μmol, CH_4 of 0.99 μmol and H_2 of 1.30 μmol under UV-visible light irradiation for 10 h, which was higher than that of the pure TiO_2 (3.58 μmol of CO, 0.60 μmol of CH_4 and 0.63 μmol of H_2) and Co-ZIF-9 (no CO, CH_4 or H_2 was detected). $ZIF_{0.03}$/T also had a better photocatalytic performance than the physical mixture of TiO_2 and Co-ZIF-9 at the same mass ratio of 0.03:0.97 (where 3.86 μmol of CO, 0.42 μmol of CH_4, and 0.56 μmol of H_2 were produced) due to the better charge separation. It was found that when the mass ratios of Co-ZIF-9 was higher than 0.1, the photocatalytic activity decreased with increasing the Co-ZIF-9 content in ZIF_x/T, which might be

attributed to the heavier charge recombination.

Pipelzadeh et al. [140] reported the CO_2 photoreduction to CH_4 and CO over a ZIF-8/TiO_2 composite with core-shell structure in a photoreactor equipped with simulated sunlight at a constant pressure (CP, 5 bar) and an intentionally controlled pressure swing (PS) at 50 mL/min (PS-50) and 100 mL/min (PS-100). A high CO yield was achieved in the PS mode at a production rate of 13.2 μmol/(g·h) (PS-50, 80% increase than CP-50 operation) and 15.6 μmol/(g·h) (PS-100, 30% increase than CP-100). The PS mode had a better promotion effect on CO production than CH_4. Continuous alteration of the reactants and product adsorption/desorption over the photocatalyst in the PS mode was beneficial to the regeneration of Ti^{3+} active sites, which contributed to the enhancement of photoreduction activity [17]. In addition, a higher gas flow rate facilitated CO removal to avoid catalyst poisoning. The calcination of ZIF-8/TiO_2 composite at 300°C further increased the yield of CO with 45.16 μmol/(g·h) under PS-100 condition, which was higher than that observed in the CP-100 mode (33.46 μmol/(g·h)) because of the higher structural stability of the ZIF-8/TiO_2 composite.

Composite photocatalysts composed of Cu-BTC (also named as HKUST-1, BTC = benzene-1,3,5-tricarboxylate) and TiO_2 were also developed for CO_2 photocatalytic reduction. Ye and coworkers [126] synthesized a Cu-BTC/TiO_2 composite with a core-shell structure (see morphologies in Fig. 10) and evaluated the CO_2 photocatalytic performance. Under UV irradiation for 4 h, the production rate of CH_4 and H_2 from CO_2 over the bare TiO_2 reached 0.52 and 2.29 μmol/(g_{TiO_2}·h), respectively, whereas the formation rate of CH_4 over the Cu-BTC/TiO_2 composite reached 2.64 μmol/(g_{TiO_2}·h) with no H_2 detected. No product was produced over Cu-BTC, because its conjugated structure did not favor charge separation. This indicates that the CH_4 yield and the selectivity of CH_4 to H_2 over Cu-BTC/TiO_2 composite are significantly improved compared to the bare TiO_2 and Cu-BTC in photocatalytic reduction. Under UV irradiation, the TiO_2 in Cu-BTC/TiO_2 composite is photoexcited to generate charge pairs and the electrons can be effectively transferred to Cu-BTC, as demonstrated by the ultrafast spectroscopy. This facilitates the charge separation in TiO_2 and supplies active electrons to CO_2 molecules adsorbed on Cu-BTC, leading to an enhancement in photocatalytic activity of Cu-BTC/TiO_2 composite. Theoretical simulations demonstrate that the activation-energy barrier for CO_2 on the Cu sites in Cu-BTC will be lowered upon receiving the photo-excited electrons from TiO_2, enabling the CO_2 reduction occurring on the Cu sites of Cu-BTC and the enhanced selectivity of CH_4 to H_2 production. Lately, Wang and coworkers [127] synthesized Cu-BTC/TiO_2 composites in microdroplets via an aerosol route. Similarly, Cu-BTC/TiO_2 composites had a higher photocatalytic performance than the pure TiO_2 and Cu-BTC. The yield of CO from CO_2 conversion over Cu-BTC/TiO_2 composites increased as a function of the molar ratio of Cu-BTC to TiO_2 ranging from 0 (i.e., bare TiO_2) to 3.33 (see Fig. 11), where the production rate of CO over 3.33Cu-BTC/TiO_2 increased to 256.35 μmol/(g_{TiO_2}·h) as compared to the bare TiO_2 with a CO formation rate of 11.48 μmol/(g_{TiO_2}·h). As demonstrated by the *in situ* diffuse reflectance infrared Fourier transform spectrometer (DRIFTS) analysis, the enhancement in the photoreduction performance of the Cu-BTC/TiO_2 composites may have been caused by the improved adsorption of reactants on the catalyst.

In addition to ZIF and Cu-based MOFs, TiO_2 was also incorporated into other MOF structures to form MOF-TiO_2 composites for CO_2 photoreduction. Li and coworkers [128] combined TiO_2 with CPO-27-Mg (also named as Mg_2(DOBDC), DOBDC = 2,5-dioxido-1,4-benzenedicarboxylate) to produce a CPO-27-Mg/TiO_2 composite via a hydrothermal self-assembly method. There exists a high concentration of open alkaline metal sites (Mg^{2+}) in CPO-27-Mg structure, endowing the high CO_2 adsorption capacity of CPO-27-Mg. Under UV irradiation for 10 h, 40.9 μmol/g of CO and 23.5 μmol/g of CH_4 were produced over CPO-27-Mg/TiO_2, which were higher than those observed over pure TiO_2 (22.5 μmol/g of CO and 13.7 μmol/g of CH_4). The enhanced performance of CPO-27-Mg/TiO_2 composite on CO_2 photoreduction is

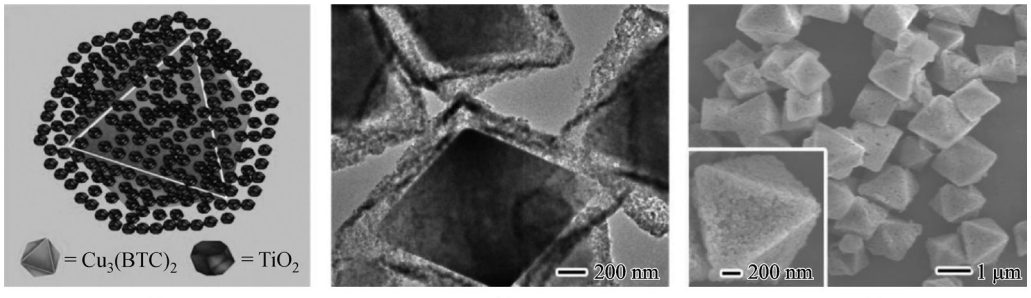

Fig. 10 Core-shell structures of Cu(BTC)/TiO_2

(a) Structural illustration; (b) transmission electron microscope (TEM); (c) SEM images of Cu(BTC)/TiO_2 core-shell structures (Reproduced with permission from Ref. [126]. Copyright 2014, Wiley)

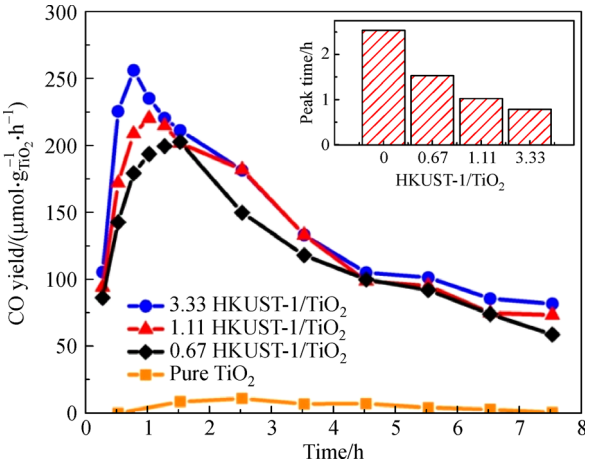

Fig. 11 CO_2 photoreduction analysis of TiO_2 and HKUST-1/TiO_2 composites (CO yield over the HKUST-1/TiO_2 composites and pure TiO_2). Inset image: CO yield peak time of the HKUST-1/TiO_2 composites and pure TiO_2 (Reproduced with permission from Ref. [127]. Copyright 2017, American Chemical Society)

attributed to its high CO_2 adsorption capacity and the existence of open Mg^{2+} metal sites. The CO_2 photoreduction over a physical mixture of TiO_2 and CPO-27-Mg (the ratio of TiO_2 to CPO-27-Mg was 6:4.) was also performed under the similar condition, and 8.5 μmol/g of H_2, 18.9 μmol/g of CO, and 7.1 μmol/g of CH_4 were produced, which were lower than those produced over the CPO-27-Mg/TiO_2 composite. This demonstrates the indispensable effect of the strong interaction between CPO-27-Mg and TiO_2 in CPO-27-Mg/TiO_2 composite for the CO_2 photoreduction. TiO_2 nanosheets were coupled with NH_2-UiO-66 using an *in situ* growth strategy by Petit and coworkers [129]. The content of NH_2-UiO-66 in the composite was varied from 19 wt% to 37 wt%. NH_2-UiO-66/TiO_2 had a better performance in photo reducing CO_2 to CO than their single moiety. This improvement is a result of the enhanced abundance of long-lived charge carriers and high CO_2 adsorption capacity in NH_2-UiO-66/TiO_2 composites.

3.2.2 MOF-CdS composites

CdS semiconductor has been widely used for CO_2 photoreduction as a photocatalyst [141–143]. Wang et al. [130] incorporated CdS into Co-ZIF-9 and the as-obtained Co-ZIF-9/CdS composite had a good photocatalytic activity toward CO_2 conversion to CO under visible light irradiation. CO_2 photoreduction was performed in MeCN and H_2O solvent with TEOA as a sacrificial agent and bipyridine (bpy) as an assistant for electron transfer. After visible light irradiation for 1 h, 50.4 μmol of CO and 11.1 μmol of H_2 were produced over Co-ZIF-9/CdS composite, which outperformed its counterparts with lower yields of CO and H_2 and pure CdS semiconductor (0.5 μmol of CO and 1.6 μmol of H_2) under the same condition (as shown in Table 3). The photocatalytic mechanism was proposed as follows: under visible light irradiation, the CdS semiconductor was excited and charge carriers were generated. The photo-generated electrons transferred to Co-ZIF-9 and reduced the CO_2 molecules adsorbed on Co-ZIF-9 to CO. Meanwhile the protons existed in the reaction system were also reduced to H_2 by the excited electrons. Lately, Su et al. [55] prepared a series of UiO-66-NH_2/$Cd_{0.2}Zn_{0.8}S$ composites with different UiO-66-NH_2 contents using a solvothermal method. CO_2 photoreduction was performed over UiO-66-NH_2/$Cd_{0.2}Zn_{0.8}S$ composites under visible light irradiation, which all had an enhanced photocatalytic activity in comparison to their single components. The UiO-66-NH_2/$Cd_{0.2}Zn_{0.8}S$ composite with a UiO-66-NH_2 content of 20 wt% had the best photocatalytic performance with a H_2 production rate of 5846.5 μmol/(g·h) and a CH_3OH production rate of 6.8 μmol/(g·h). The efficient charge separation and transfer between $Cd_{0.2}Zn_{0.8}S$ and UiO-66-NH_2 contributed to the enhanced photocatalytic activity of UiO-66-NH_2/$Cd_{0.2}Zn_{0.8}S$ composites.

3.2.3 MOF-graphitic C_3N_4 composites

Graphitic carbon nitrides (g-C_3N_4) with different morphologies and structures have been integrated with MOFs to improve the CO_2 photoreduction activity. Wang and coworkers [131] coupled mesoporous g-C_3N_4 with Co-ZIF-9, which acted as a light harvester and co-catalyst, respectively, to fabricate a Co-ZIF-9/g-C_3N_4 composite. The Co-ZIF-9/g-C_3N_4 composite efficiently catalyzed CO_2 to CO and H_2 under visible light irradiation. 20.8 μmol of CO and 3.3 μmol of H_2 were obtained over the Co-ZIF-9/g-C_3N_4 composite in 2 h, whereas no product was detected over the pristine Co-ZIF-9 and g-C_3N_4. Liu and coworkers [56] developed a series of ZIF-8/g-C_3N_4 composites by growing different contents of ZIF-8 nanoclusters on the surface of g-C_3N_4 nanotubes. The ZIF-8/g-C_3N_4 composites had an increased CO_2 adsorption capacity than g-C_3N_4 nanotubes without sacrificing the light absorption capacity owing to the incorporation of ZIF-8 nanoclusters. Because of the high CO_2 capture capacity of ZIF-8 and the promoted charge separation efficiency from the g-C_3N_4 nanotubes, the ZIF-8/g-C_3N_4 composites had an enhanced photocatalytic performance on CO_2 reduction, where the highest production rate of methanol reached 0.75 μmol/(g·h) over the ZIF-8/g-C_3N_4 composite in which the mass ratio of g-C_3N_4 nanotubes to ZIF-8 was 8 under light irradiation for 1 h. Under similar conditions, g-C_3N_4 nanotubes and bulk g-C_3N_4 had a production rate of methanol of 0.49 and 0.24 μmol/(g·h), respectively, whereas no methanol was produced over the pure ZIF-8 nanocrystals. In addition, g-C_3N_4 nanosheets were com-

bined with UiO-66 [132] and BIF-20 (a zeolite-like porous boron imidazolate framework) [133] MOFs to form MOF/g-C_3N_4 composites, which all had an enhanced performance on CO_2 photocatalytic reduction.

In addition to TiO_2, CdS and C_3N_4, another type of semiconductor was also incorporated into MOFs to generate a composite photocatalyst for CO_2 photocatalytic reduction. Wang and coworkers [134] developed a ZIF-8/Zn_2GeO_4 composite by growing ZIF-8 nanoparticles on Zn_2GeO_4 nanorods. The ZIF-8/Zn_2GeO_4 composite inherited both the high CO_2 adsorption capacity of ZIF-8 nanoparticles and the high crystallinity of Zn_2GeO_4 nanorods. The ZIF-8/Zn_2GeO_4 composite with 25 wt% ZIF-8 had a CO_2 adsorption capacity of 15.5 cm^3/g, which was higher than the pure Zn_2GeO_4 nanorods (4.9 cm^3/g) due to the high CO_2 adsorption ability of ZIF-8. After 11 h of light irradiation in Na_2SO_3, the production of methanol at a rate of 0.22 μmol/(g·h) over the ZIF-8(25wt%)/Zn_2GeO_4 composite was observed. The yield of methanol over the ZIF-8(25 wt%)/Zn_2GeO_4 composite had a 62% increase in comparison to the pure Zn_2GeO_4 nanorods under light irradiation for 10 h. The enhanced CO_2 photoreduction performance of ZIF-8/Zn_2GeO_4 composite may have been resulted from the high CO_2 adsorption capacity of ZIF-8 and the higher light response.

3.3 MOF composites incorporated with metals

Because of their high Fermi energy levels, noble metal nanoparticles can effectively separate photo-generated charge pairs of photocatalysts [144,145]. Therefore, another approach to promoting the CO_2 photocatalytic reduction is to dope noble metal nanoparticles into MOF structures to decrease the recombination rate of the photo-generated electrons and holes. Li and coworkers [135] synthesized M-doped NH_2-MIL-125(Ti) (M = Pt and Au) and conducted CO_2 photocatalytic reaction in saturated CO_2 with TEOA as a sacrificial agent under visible light irradiation. Both H_2 and $HCOO^-$ were produced over M/NH_2-MIL-125(Ti), while no H_2 but only $HCOO^-$ was produced over bare NH_2-MIL-125(Ti). The reason for this is that the electron-trapping effect of noble metals promotes the hydrogen evolution. In addition, it is noted that Pt and Au had different photocatalytic performances on the production of $HCOO^-$. Compared to bare NH_2-MIL-125(Ti) (yield of $HCOO^-$: 10.75 μmol), Pt/NH_2-MIL-125(Ti) had a higher production yield of $HCOO^-$ (12.96 μmol), while Au/NH_2-MIL-125(Ti) had a lower production of $HCOO^-$ (9.06 μmol) under visible light irradiation for 8 h. As demonstrated by electron spin resonance (ESR) studies and density functional theory (DFT) calculations, hydrogen spillover from Pt to the bridging oxygen linked to Ti atoms occurred in Pt/NH_2-MIL-125(Ti), leading to the Ti^{3+} formation and boosting the hydrogen-assisted CO_2 reduction to $HCOO^-$. In contrast, it was difficult to achieve the hydrogen spillover from Au to the NH_2-MIL-125(Ti) framework in Au/NH_2-MIL-125(Ti), and thus resulting in a lower $HCOO^-$ formation over Au/NH_2-MIL-125(Ti). Fu et al. [136] doped different contents of Co (from 1 to 3 wt%) into NH_2-MIL-125(Ti) and produced Co/NH_2-MIL-125(Ti) composites for CO_2 photoreduction under visible light irradiation. 1 wt% Co/NH_2-MIL-125(Ti) had the best performance on CO_2 photoreduction with an $HCOO^-$ formation of 384.2 μmol in 10 h, which was 2-fold higher than that observed over pure NH_2-MIL-125(Ti) (162.8 μmol) due to the enhanced visible-light harvesting and electron transfer stemmed from the addition of Co.

Yaghi and coworkers [137] functionalized UiO-67 with Re complexes, $Re^I(CO)_3$(5,5′-dcbpy)Cl photosensitizer, of various densities (Re_n-MOF, n = 0, 1, 2, 3, 5, 11, 16, and 24 complexes per unit cell) and found that the photocatalytic activity of the MOF system can be controlled by controlling the density of Re complexes in the framework, in which Re_3-MOF had the best performance on CO_2-to-CO conversion. The photocatalytic activity was further enhanced by coating a 16 nm layer of Re_3-MOF onto Ag nanocubes (Ag⊂Re_3-MOF, see Fig. 12), where a 7-fold improvement of CO_2-to-CO reduction compared to pure Re_3-MOF under visible light irradiation was achieved. Both Re complexes and Ag nanocubes contributed to the CO_2 photocatalytic activity enhancement of Ag⊂Re_3-MOF. Because the quadrupolar localized surface plasmon resonance (LSPR) scattering peak (λ_{max}~ 480 nm) of Ag nanocube overlapped with the absorption range of $Re^I(CO)_3$(5,5′-dcbpy)Cl (400 nm < λ < 550 nm) in the visible region [146,147] and Ag⊂Re_3-MOF structure inherited the LSPR features of Ag cores, the photoactive Re metal sites within MOF shell were spatially localized into a strong electromagnetic field induced by LSPR of the Ag nanocubes for photocatalytic enhancement.

3.4 MOF composites incorporated with carbon materials

Another important strategy to develop active photocatalysts for CO_2 photoreduction is the incorporation of carbon materials such as graphene and its derivatives into MOFs. Graphene can act as a photosensitizer to extend the light adsorption region from the UV to the visible light region. Moreover, the excellent conductivity of graphene can facilitate the rapid transfer of the photo-generated electrons and suppress the electron-hole recombination, and subsequently boost the photocatalytic activity.

Li and coworkers [138] synthesized UiO-66-NH_2/graphene composites via microwave-assisted *in situ* growth of different amounts (1–3 wt%) of UiO-66-NH_2 nanocrystals onto graphene. As compared to the pure UiO-66-NH_2 (3.1 μmol of $HCOO^-$, 0.11 μmol of CH_4, and 16.9 μmol of H_2 were produced.) and the UiO-66-NH_2/graphene synthesized via a traditional hydrothermal route (16.1 μmol of $HCOO^-$ and 20.4 μmol of H_2 were produced.), the as-obtained UiO-66-NH_2/graphene com-

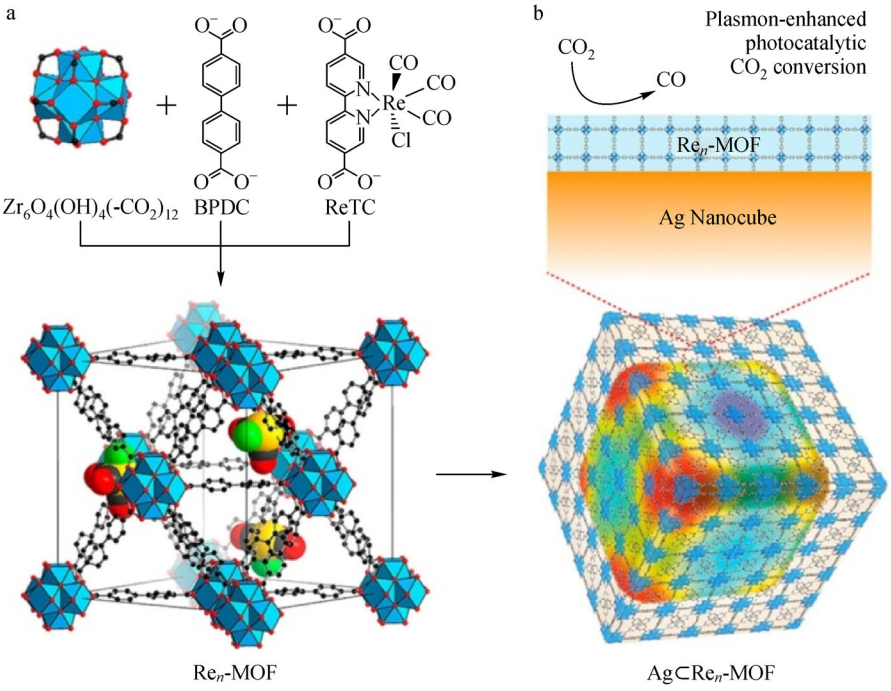

Fig. 12 Structures of Re_n-MOF and Ag⊂Re_n-MOF for plasmon-enhanced photocatalytic CO_2 conversion
(a) Structure of Re_n-MOF (C: black; O: red; Zr: blue polyhedra; Re: yellow; Cl: green; H atoms are omitted for clarity); (b) Re_n-MOF coated on a Ag nanocube for CO_2 photoreduction enhancement (Reproduced with permission from Ref. [137]. Copyright 2017, American Chemical Society)

posites had a better performance on CO_2 photoreduction activity and selectivity under visible light irradiation. Of the UiO-66-NH_2/graphene composites as prepared, 2 wt% UiO-66-NH_2/graphene composite had the best performance, where 33.5 μmol of $HCOO^-$, 0.9 μmol of CH_4 and 13.2 μmol of H_2 were produced in 4 h. The performance enhancement is attributed to both the fine particle size and high dispersion of UiO-66-NH_2 nanocrystals, which enables more light trapping to generate charge pairs and shortens the electron transfer pathway to facilitate electron transfer. Additionally, the strong UiO-66-NH_2/graphene interaction can also effectively accelerate electron transfer efficiency to enhance photocatalytic activity for CO_2 reduction.

Do and coworkers [139] incorporated different contents of amine-functionalized reduced graphene oxide (NH_2-rGO) (5–25 wt%) into a TCPP-based MOF (Al/PMOF) to form Al-PMOF/NH_2-rGO composites as photocatalysts for CO_2 reduction. Al-PMOF/NH_2-rGO composites had an enhanced photocatalytic activity for CO_2 reduction, where the $HCOO^-$ formation rate reached 685.6 μmol /(g·h) over Al-PMOF/5 wt% NH_2-rGO under visible light irradiation in 6 h, which was much higher than the $HCOO^-$ production rate observed over pure Al-PMOF (165.3 μmol /(g·h)). The photocatalytic mechanism is proposed as follows: upon visible light irradiation, TCPP is responsible for light harvesting and is excited to produce photo-generated electron-hole pairs, and the electrons are transferred from TCPP to graphene which acts as an electron acceptor. The electrons transferred from graphene reduce the adsorbed CO_2 to $HCOO^-$ in the presence of TEOA that serves as a hydrogen source.

Most recently, MOF with a special microstructure in CO_2 photoreduction was reported. Lin and coworkers [148] prepared Ni-based MOF ($Ni_2(OH)_2BDC$) monolayers (Ni MOLs) and examined the performance for photoreduction of CO_2 under visible light irradiation with $[Ru(bpy)_3]Cl_2 \cdot 6H_2O$ as a photosensitizer and TEOA as an electron donor. After 2 h reaction in pure CO_2, Ni MOLs had a CO production rate of 12.5 μmol/h and a H_2 production rate of 0.28 μmol/h, whereas bulk Ni MOFs had a lower CO production rate of 7.23 μmol/h. In diluted CO_2, Ni MOLs had a CO selectivity of 96.8 %, which outperformed most of the reported systems in diluted CO_2. It was proposed that the strong affinity of Ni MOLs to CO_2 molecules enabled their high CO_2 adsorption ability and stabilized the initial Ni-CO_2 adducts, thus promoting CO_2-to-CO conversion. In addition, weak affinity of Ni MOLs to H_2O impeded the transfer of protons, thereby reducing the H_2 formation.

4 Conclusions and outlook

In recent years, MOFs have attracted great attention and showed much potential as photocatalysts for CO_2 reduction because of their super-high surface areas, tunable structures, and high CO_2 adsorption capacity. This review

summarizes the recent research progresses in the development of MOFs and MOF-based composite photocatalysts for the photocatalytic reduction of CO_2. Several strategies in improving light harvesting, CO_2 adsorption and charge separation have been discussed, which provides guidelines for rational design of MOF-based photocatalysts with enhanced performance on CO_2 reduction under visible light irradiation. Although great progress has been made in the development of MOF-based photocatalysts for CO_2 reduction, there still exist some challenges and large potential need to be explored. For instance, ① to date several thousands of MOFs with different structures have been developed, however, only several types of MOFs such as ZIFs, UiO- and MIL-based MOFs are under exploration as photocatalysts for CO_2 reduction. More efforts need to be made in investigation of many other MOF systems with active catalytic centers, which may be promising for photocatalysis. ② Most MOFs have a poor stability in aqueous solution and suffer structural collapse, which limit their practical applications in catalysis processes where water is involved. Therefore, it is imperative to develop novel MOF photocatalysts which have an excellent chemical stability in aqueous solution and meanwhile retain the photocatalytic functionality. ③ The current research achievements in photocatalytic reduction of CO_2 over MOF-based photocatalysts have not yet met the requirement for large-scale industrial applications, therefore, exploration in further improvement of CO_2 photoreduction is required. So far, many novel materials such as two-dimensional (2D) nanomaterials like graphene and 2D semiconductors have been developed; integrating these novel nanomaterials into MOF structures may be considered as a promising strategy to enhance the photocatalytic performance of MOFs. It is believed that with the rapid development progress of MOF materials and other novel photocatalytic materials, MOF-based photocatalysts will have even greater potential to fulfill the requirements for practical applications in heterogeneous photocatalysis in the future.

Acknowledgements This work was supported by a startup fund from the University of Alaska Fairbanks.

References

1. Pearson P N, Palmer M R. Atmospheric carbon dioxide concentrations over the past 60 million years. Nature, 2000, 406 (6797): 406695
2. Quadrelli R, Peterson S. The energy–climate challenge: recent trends in CO_2 emissions from fuel combustion. Energy Policy, 2007, 35(11): 5938–5952
3. Song C. CO_2 conversion and utilization: an overview. In: Song C, eds. CO_2 Conversion and Utilization. Washington, DC: ACS Symposium Series, 2002, 809, 2–30
4. Herzog H J, Drake E M. Carbon dioxide recovery and disposal from large energy systems. Annual Review of Energy and the Environment, 1996, 21(1): 145–166
5. Muradov N. Industrial Utilization of CO_2: A Win–Win Solution. New York: Springer New York, 2014, 325–383
6. Rafiee A, Rajab Khalilpour K, Milani D, Panahi M. Trends in CO_2 conversion and utilization: a review from process systems perspective. Journal of Environmental Chemical Engineering, 2018, 6(5): 5771–5794
7. Wang B, Chen W, Song Y, Li G, Wei W, Fang J, Sun Y. Recent progress in the photocatalytic reduction of aqueous carbon dioxide. Catalysis Today, 2018, 311: 23–39
8. Yu Y, Zheng W, Cao Y. TiO_2–Pd/C composited photocatalyst with improved photocatalytic activity for photoreduction of CO_2 into CH_4. New Journal of Chemistry, 2017, 41(8): 3204–3210
9. Sneddon G, Greenaway A, Yiu H H P. The potential applications of nanoporous materials for the adsorption, separation, and catalytic conversion of carbon dioxide. Advanced Energy Materials, 2014, 4(10): 1301873
10. North M, Pasquale R, Young C. Synthesis of cyclic carbonates from epoxides and CO_2. Green Chemistry, 2010, 12(9): 1514–1539
11. Li W, Wang H, Jiang X, Zhu J, Liu Z, Guo X, Song C. A short review of recent advances in CO_2 hydrogenation to hydrocarbons over heterogeneous catalysts. RSC Advances, 2018, 8(14): 7651–7669
12. Raciti D, Wang C. Recent advances in CO_2 reduction electrocatalysis on copper. ACS Energy Letters, 2018, 3(7): 1545–1556
13. Tahir M, Amin N S. Advances in visible light responsive titanium oxide-based photocatalysts for CO_2 conversion to hydrocarbon fuels. Energy Conversion and Management, 2013, 76: 194–214
14. Matsubara Y, Grills D C, Kuwahara Y. Thermodynamic aspects of electrocatalytic CO_2 reduction in acetonitrile and with an ionic liquid as solvent or electrolyte. ACS Catalysis, 2015, 5(11): 6440–6452
15. Fujishima A, Honda K. Electrochemical photolysis of water at a semiconductor electrode. Nature, 1972, 238(5358): 23837
16. Wang M, Ioccozia J, Sun L, Lin C, Lin Z. Inorganic-modified semiconductor TiO_2 nanotube arrays for photocatalysis. Energy & Environmental Science, 2014, 7(7): 2182–2202
17. Bao N, Shen L, Takata T, Domen K. Self-templated synthesis of nanoporous CdS nanostructures for highly efficient photocatalytic hydrogen production under visible light. Chemistry of Materials, 2008, 20(1): 110–117
18. Ong C B, Ng L Y, Mohammad A W. A review of ZnO nanoparticles as solar photocatalysts: synthesis, mechanisms and applications. Renewable & Sustainable Energy Reviews, 2018, 81: 536–551
19. Lee G J, Wu J J. Recent developments in ZnS photocatalysts from synthesis to photocatalytic applications—a review. Powder Technology, 2017, 318: 8–22
20. Mishra M, Chun D M. α-Fe_2O_3 as a photocatalytic material: a review. Applied Catalysis A, General, 2015, 498: 126–141
21. Wen J, Xie J, Chen X, Li X. A review on g-C_3N_4-based photocatalysts. Applied Surface Science, 2017, 391: 72–123
22. Luo L, Li Y, Hou J, Yang Y. Visible photocatalysis and photostability of Ag_3PO_4 photocatalyst. Applied Surface Science,

2014, 319: 332–338
23. Dong C, Lian C, Hu S, Deng Z, Gong J, Li M, Liu H, Xing M, Zhang J. Size-dependent activity and selectivity of carbon dioxide photocatalytic reduction over platinum nanoparticles. Nature Communications, 2018, 9(1): 1252
24. Xing M, Zhou Y, Dong C, Cai L, Zeng L, Shen B, Pan L, Dong C, Chai Y, Zhang J, Yin Y. Modulation of the reduction potential of TiO_{2-x} by fluorination for efficient and selective CH_4 generation from CO_2 photoreduction. Nano Letters, 2018, 18(6): 3384–3390
25. Zhang H, Liu G, Shi L, Liu H, Wang T, Ye J. Engineering coordination polymers for photocatalysis. Nano Energy, 2016, 22: 149–168
26. Meissner D, Memming R, Kastening B. Photoelectrochemistry of cadmium sulfide. 1. Reanalysis of photocorrosion and flat-band potential. Journal of Physical Chemistry, 1988, 92(12): 3476–3483
27. Bahnemann D W, Kormann C, Hoffmann M R. Preparation and characterization of quantum size zinc oxide: a detailed spectroscopic study. Journal of Physical Chemistry, 1987, 91(14): 3789–3798
28. Zhang L, Hu Y H. Desorption of dimethylformamide from $Zn_4O(C_8H_4O_4)_3$ framework. Applied Surface Science, 2011, 257(8): 3392–3398
29. Hu Y H, Zhang L. Amorphization of metal-organic framework MOF-5 at unusually low applied pressure. Physical Review. B, 2010, 81(17): 174103
30. Zhang L, Hu Y H. A systematic investigation of decomposition of nano $Zn_4O(C_8H_4O_4)_3$ metal–organic framework. Journal of Physical Chemistry C, 2010, 114(6): 2566–2572
31. Zhang L, Hu Y H. Strong effects of higher-valent cations on the structure of the zeolitic Zn(2-methylimidazole)$_2$ framework (ZIF-8). Journal of Physical Chemistry C, 2011, 115(16): 7967–7971
32. Zhang L, Hu Y H. Structure distortion of $Zn_4O_{13}C_{24}H_{12}$ framework (MOF-5). Materials Science and Engineering B, 2011, 176 (7): 573–578
33. Zhang L, Hu Y H. Observation of ZnO nanoparticles outside pores of nano $Zn_4O(C_8H_4O_4)_3$ metal–organic framework. Physics Letters [Part A], 2011, 375(13): 1514–1517
34. Loera-Serna S, Zarate-Rubio J, Medina-Velazquez D Y, Zhang L, Ortiz E. Encapsulation of urea and caffeine in $Cu_3(BTC)_2$ metal–organic framework. Surface Innovations, 2016, 4(2): 76–87
35. Hu Y H, Zhang L. Hydrogen storage in metal–organic frameworks. Advanced Materials, 2010, 22(20): E117–E130
36. Zhang T, Lin W. Metal–organic frameworks for artificial photosynthesis and photocatalysis. Chemical Society Reviews, 2014, 43(16): 5982–5993
37. Wu M X, Yang Y W. Metal–organic framework (MOF)-based drug/cargo delivery and cancer therapy. Advanced Materials, 2017, 29(23): 1606134
38. Chowdhury T, Zhang L, Zhang J, Aggarwal S. Removal of arsenic (III) from aqueous solution using metal organic framework-graphene oxide nanocomposite. Nanomaterials (Basel, Switzerland), 2018, 8(12): 1062
39. Kreno L E, Leong K, Farha O K, Allendorf M, Van Duyne R P, Hupp J T. Metal–organic framework materials as chemical sensors. Chemical Reviews, 2012, 112(2): 1105–1125
40. Wang Y, Huang N Y, Shen J Q, Liao P Q, Chen X M, Zhang J P. Hydroxide ligands cooperate with catalytic centers in metal–organic frameworks for efficient photocatalytic CO_2 reduction. Journal of the American Chemical Society, 2018, 140(1): 38–41
41. He J, Zhang Y, He J, Zeng X, Hou X, Long Z. Enhancement of photoredox catalytic properties of porphyrinic metal–organic frameworks based on titanium incorporation via post-synthetic modification. Chemical Communications, 2018, 54(62): 8610–8613
42. Horiuchi Y, Toyao T, Saito M, Mochizuki K, Iwata M, Higashimura H, Anpo M, Matsuoka M. Visible-light-promoted photocatalytic hydrogen production by using an amino-functionalized Ti(IV) metal–organic framework. Journal of Physical Chemistry C, 2012, 116(39): 20848–20853
43. Maina J W, Pozo-Gonzalo C, Kong L, Schütz J, Hill M, Dumée L F. Metal organic framework based catalysts for CO_2 conversion. Materials Horizons, 2017, 4(3): 345–361
44. Nasalevich M A, Goesten M G, Savenije T J, Kapteijn F, Gascon J. Enhancing optical absorption of metal–organic frameworks for improved visible light photocatalysis. Chemical Communications, 2013, 49(90): 10575–10577
45. Jiang D, Mallat T, Krumeich F, Baiker A. Copper-based metal-organic framework for the facile ring-opening of epoxides. Journal of Catalysis, 2008, 257(2): 390–395
46. Hasegawa S, Horike S, Matsuda R, Furukawa S, Mochizuki K, Kinoshita Y, Kitagawa S. Three-dimensional porous coordination polymer functionalized with amide groups based on tridentate ligand: selective sorption and catalysis. Journal of the American Chemical Society, 2007, 129(9): 2607–2614
47. Wang J L, Wang C, Lin W. Metal–organic frameworks for light harvesting and photocatalysis. ACS Catalysis, 2012, 2(12): 2630–2640
48. Llabrés i Xamena F X, Casanova O, Galiasso Tailleur R, Garcia H, Corma A. Metal organic frameworks (MOFs) as catalysts: a combination of Cu^{2+} and Co^{2+} MOFs as an efficient catalyst for tetralin oxidation. Journal of Catalysis, 2008, 255(2): 220–227
49. Llabrés i Xamena F X, Corma A, Garcia H. Applications for metal–organic frameworks (MOFs) as quantum dot semiconductors. Journal of Physical Chemistry C, 2007, 111(1): 80–85
50. Gao J, Miao J, Li P Z, Teng W Y, Yang L, Zhao Y, Liu B, Zhang Q. A p-type Ti(iv)-based metal–organic framework with visible-light photo-response. Chemical Communications, 2014, 50(29): 3786–3788
51. Shen L, Liang S, Wu W, Liang R, Wu L. CdS-decorated UiO-66 (NH_2) nanocomposites fabricated by a facile photodeposition process: an efficient and stable visible-light-driven photocatalyst for selective oxidation of alcohols. Journal of Materials Chemistry. A, 2013, 1(37): 11473–11482
52. Ryu U J, Kim S J, Lim H K, Kim H, Choi K M, Kang J K. Synergistic interaction of Re complex and amine functionalized multiple ligands in metal-organic frameworks for conversion of carbon dioxide. Scientific Reports, 2017, 7(1): 612
53. Fu Y, Sun D, Chen Y, Huang R, Ding Z, Fu X, Li Z. An amine-functionalized titanium metal–organic framework photocatalyst with visible-light-induced activity for CO_2 reduction. Angewandte Chemie International Edition, 2012, 51(14): 3364–3367
54. Yan S, Ouyang S, Xu H, Zhao M, Zhang X, Ye J. Co-ZIF-9/TiO_2

nanostructure for superior CO_2 photoreduction activity. Journal of Materials Chemistry. A, 2016, 4(39): 15126–15133
55. Su Y, Zhang Z, Liu H, Wang Y. $Cd_{0.2}Zn_{0.8}S$@UiO-66–NH_2 nanocomposites as efficient and stable visible-light-driven photocatalyst for H_2 evolution and CO_2 reduction. Applied Catalysis B: Environmental, 2017, 200: 448–457
56. Liu S, Chen F, Li S, Peng X, Xiong Y. Enhanced photocatalytic conversion of greenhouse gas CO_2 into solar fuels over g-C_3N_4 nanotubes with decorated transparent ZIF-8 nanoclusters. Applied Catalysis B: Environmental, 2017, 211: 1–10
57. Wang S, Yao W, Lin J, Ding Z, Wang X. Cobalt imidazolate metal–organic frameworks photosplit CO_2 under mild reaction conditions. Angewandte Chemie International Edition, 2014, 53(4): 1034–1038
58. Fei H, Sampson M D, Lee Y, Kubiak C P, Cohen S M. Photocatalytic CO_2 reduction to formate using a Mn(I) molecular catalyst in a robust metal–organic framework. Inorganic Chemistry, 2015, 54(14): 6821–6828
59. Qin J, Wang S, Wang X. Visible-light reduction CO_2 with dodecahedral zeolitic imidazolate framework ZIF-67 as an efficient co-catalyst. Applied Catalysis B: Environmental, 2017, 209: 476–482
60. Huang Y B, Liang J, Wang X S, Cao R. Multifunctional metal–organic framework catalysts: synergistic catalysis and tandem reactions. Chemical Society Reviews, 2017, 46(1): 126–157
61. Wang S, Wang X. Multifunctional metal–organic frameworks for photocatalysis. Small, 2015, 11(26): 3097–3112
62. Yu X, Wang L, Cohen S M. Photocatalytic metal–organic frameworks for organic transformations. CrystEngComm, 2017, 19(29): 4126–4136
63. Navarro Amador R, Carboni M, Meyer D. Photosensitive titanium and zirconium metal organic frameworks: current research and future possibilities. Materials Letters, 2016, 166: 327–338
64. Liang Z, Qu C, Guo W, Zou R, Xu Q. Pristine metal–organic frameworks and their composites for energy storage and conversion. Advanced Materials, 2018, 30(37): 1702891
65. Sun D, Li Z. Robust Ti- and Zr-based metal-organic frameworks for photocatalysis. Chinese Journal of Chemistry, 2017, 35(2): 135–147
66. Shen L, Liang R, Wu L. Strategies for engineering metal-organic frameworks as efficient photocatalysts. Chinese Journal of Catalysis, 2015, 36(12): 2071–2088
67. Zhu J, Li P Z, Guo W, Zhao Y, Zou R. Titanium-based metal–organic frameworks for photocatalytic applications. Coordination Chemistry Reviews, 2018, 359: 80–101
68. Santaclara J G, Kapteijn F, Gascon J, van der Veen M A. Understanding metal–organic frameworks for photocatalytic solar fuel production. CrystEngComm, 2017, 19(29): 4118–4125
69. Nasalevich M A, van der Veen M, Kapteijn F, Gascon J. Metal–organic frameworks as heterogeneous photocatalysts: advantages and challenges. CrystEngComm, 2014, 16(23): 4919–4926
70. Song F, Li W, Sun Y. Metal–organic frameworks and their derivatives for photocatalytic water splitting. Inorganics, 2017, 5 (3): 40
71. Wang W, Xu X, Zhou W, Shao Z. Recent progress in metal-organic frameworks for applications in electrocatalytic and photocatalytic water splitting. Advancement of Science, 2017, 4(4): 1600371
72. Yan Y, He T, Zhao B, Qi K, Liu H, Xia B Y. Metal/covalent–organic frameworks-based electrocatalysts for water splitting. Journal of Materials Chemistry. A, 2018, 6(33): 15905–15926
73. Meyer K, Ranocchiari M, van Bokhoven J A. Metal organic frameworks for photo-catalytic water splitting. Energy & Environmental Science, 2015, 8(7): 1923–1937
74. Pi Y, Li X, Xia Q, Wu J, Li Y, Xiao J, Li Z. Adsorptive and photocatalytic removal of persistent organic pollutants (POPs) in water by metal-organic frameworks (MOFs). Chemical Engineering Journal, 2018, 337: 351–371
75. Wu Z, Yuan X, Zhang J, Wang H, Jiang L, Zeng G. Photocatalytic decontamination of wastewater containing organic dyes by metal–organic frameworks and their derivatives. ChemCatChem, 2017, 9 (1): 41–64
76. Wang C C, Li J R, Lv X L, Zhang Y Q, Guo G. Photocatalytic organic pollutants degradation in metal–organic frameworks. Energy & Environmental Science, 2014, 7(9): 2831–2867
77. Jiang D, Xu P, Wang H, Zeng G, Huang D, Chen M, Lai C, Zhang C, Wan J, Xue W. Strategies to improve metal organic frameworks photocatalyst's performance for degradation of organic pollutants. Coordination Chemistry Reviews, 2018, 376: 449–466
78. Dhakshinamoorthy A, Li Z, Garcia H. Catalysis and photocatalysis by metal organic frameworks. Chemical Society Reviews, 2018, 47(22): 8134–8172
79. Zhu B, Zou R, Xu Q. Metal–organic framework based catalysts for hydrogen evolution. Advanced Energy Materials, 2018, 8(24): 1801193
80. Fang Y, Ma Y, Zheng M, Yang P, Asiri A M, Wang X. Metal–organic frameworks for solar energy conversion by photoredox catalysis. Coordination Chemistry Reviews, 2018, 373: 83–115
81. Chen Y, Wang D, Deng X, Li Z. Metal–organic frameworks (MOFs) for photocatalytic CO_2 reduction. Catalysis Science & Technology, 2017, 7(21): 4893–4904
82. Li Y, Xu H, Ouyang S, Ye J. Metal–organic frameworks for photocatalysis. Physical Chemistry Chemical Physics, 2016, 18 (11): 7563–7572
83. Li R, Zhang W, Zhou K. Metal–organic-framework-based catalysts for photoreduction of CO_2. Advanced Materials, 2018, 30(35): 1705512
84. Wang C C, Zhang Y Q, Li J, Wang P. Photocatalytic CO_2 reduction in metal–organic frameworks: a mini review. Journal of Molecular Structure, 2015, 1083: 127–136
85. Qiu J, Zhang X, Feng Y, Zhang X, Wang H, Yao J. Modified metal-organic frameworks as photocatalysts. Applied Catalysis B: Environmental, 2018, 231: 317–342
86. Gascon J, Hernández-Alonso M D, Almeida A R, van Klink G P M, Kapteijn F, Mul G. Isoreticular MOFs as efficient photocatalysts with tunable band gap: an operando FTIR study of the photoinduced oxidation of propylene. ChemSusChem, 2008, 1 (12): 981–983
87. Barkhordarian A A, Kepert C J. Two new porous UiO-66-type zirconium frameworks: open aromatic N-donor sites and their post-synthetic methylation and metallation. Journal of Materials Chemistry. A, 2017, 5(11): 5612–5618
88. Hendon C H, Tiana D, Fontecave M, Sanchez C, D'arras L,

Sassoye C, Rozes L, Mellot-Draznieks C, Walsh A. Engineering the optical response of the Titanium-MIL-125 metal–organic framework through ligand functionalization. Journal of the American Chemical Society, 2013, 135(30): 10942–10945

89. Pham H Q, Mai T, Pham-Tran N N, Kawazoe Y, Mizuseki H, Nguyen-Manh D. Engineering of band gap in metal–organic frameworks by functionalizing organic linker: a systematic density functional theory investigation. Journal of Physical Chemistry C, 2014, 118(9): 4567–4577
90. Yang H, He X W, Wang F, Kang Y, Zhang J. Doping copper into ZIF-67 for enhancing gas uptake capacity and visible-light-driven photocatalytic degradation of organic dye. Journal of Materials Chemistry, 2012, 22(41): 21849–21851
91. Yang L M, Fang G Y, Ma J, Pushpa R, Ganz E. Halogenated MOF-5 variants show new configuration, tunable band gaps and enhanced optical response in the visible and near infrared. Physical Chemistry Chemical Physics, 2016, 18(47): 32319–32330
92. Nguyen H L, Vu T T, Le D, Doan T L H, Nguyen V Q, Phan N T S. A Titanium–organic framework: engineering of the band-gap energy for photocatalytic property enhancement. ACS Catalysis, 2017, 7(1): 338–342
93. Sun D, Fu Y, Liu W, Ye L, Wang D, Yang L, Fu X, Li Z. Studies on photocatalytic CO_2 reduction over NH_2-Uio-66(Zr) and its derivatives: towards a better understanding of photocatalysis on metal–organic frameworks. Chemistry–A European Journal, 2013, 19(42): 14279–14285
94. Lee Y, Kim S, Kang J K, Cohen S M. Photocatalytic CO_2 reduction by a mixed metal (Zr/Ti), mixed ligand metal–organic framework under visible light irradiation. Chemical Communications, 2015, 51(26): 5735–5738
95. Wang D, Huang R, Liu W, Sun D, Li Z. Fe-based MOFs for photocatalytic CO_2 reduction: role of coordination unsaturated sites and dual excitation pathways. ACS Catalysis, 2014, 4(12): 4254–4260
96. Sun D, Liu W, Qiu M, Zhang Y, Li Z. Introduction of a mediator for enhancing photocatalytic performance via post-synthetic metal exchange in metal–organic frameworks (MOFs). Chemical Communications, 2015, 51(11): 2056–2059
97. Liu J, Fan Y Z, Li X, Wei Z, Xu Y W, Zhang L, Su C Y. A porous rhodium(III)-porphyrin metal-organic framework as an efficient and selective photocatalyst for CO_2 reduction. Applied Catalysis B: Environmental, 2018, 231: 173–181
98. Sadeghi N, Sharifnia S, Sheikh Arabi M.A porphyrin-based metal organic framework for high rate photoreduction of CO_2 to CH_4 in gas phase. Journal of CO_2 Utilization, 2016, 16: 450–457
99. Liu Y, Yang Y, Sun Q, Wang Z, Huang B, Dai Y, Qin X, Zhang X. Chemical adsorption enhanced CO_2 capture and photoreduction over a copper porphyrin based metal organic framework. ACS Applied Materials & Interfaces, 2013, 5(15): 7654–7658
100. Zhang H, Wei J, Dong J, Liu G, Shi L, An P, Zhao G, Kong J, Wang X, Meng X, Zhang J, Ye J. Efficient visible-light-driven carbon dioxide reduction by a single-atom implanted metal–organic framework. Angewandte Chemie International Edition, 2016, 55(46): 14310–14314
101. Xu H Q, Hu J, Wang D, Li Z, Zhang Q, Luo Y, Yu S H, Jiang H L. Visible-light photoreduction of CO_2 in a metal–organic framework: boosting electron–hole separation via electron trap states. Journal of the American Chemical Society, 2015, 137(42): 13440–13443
102. Yan Z H, Du M H, Liu J, Jin S, Wang C, Zhuang G L, Kong X J, Long L S, Zheng L S. Photo-generated dinuclear $\{Eu(II)\}_2$ active sites for selective CO_2 reduction in a photosensitizing metal-organic framework. Nature Communications, 2018, 9(1): 3353
103. Wang C, Xie Z, deKrafft K E, Lin W. Doping metal–organic frameworks for water oxidation, carbon dioxide reduction, and organic photocatalysis. Journal of the American Chemical Society, 2011, 133(34): 13445–13454
104. Huang R, Peng Y, Wang C, Shi Z, Lin W. A rhenium-functionalized metal–organic framework as a single-site catalyst for photochemical reduction of carbon dioxide. European Journal of Inorganic Chemistry, 2016, 2016(27): 4358–4362
105. Chambers M B, Wang X, Elgrishi N, Hendon C H, Walsh A, Bonnefoy J, Canivet J, Quadrelli E A, Farrusseng D, Mellot-Draznieks C, Fontecave M. Photocatalytic carbon dioxide reduction with rhodium-based catalysts in solution and heterogenized within metal–organic frameworks. ChemSusChem, 2015, 8(4): 603–608
106. Sun D, Gao Y, Fu J, Zeng X, Chen Z, Li Z. Construction of a supported Ru complex on bifunctional MOF-253 for photocatalytic CO_2 reduction under visible light. Chemical Communications, 2015, 51(13): 2645–2648
107. Li L, Zhang S, Xu L, Wang J, Shi L X, Chen Z N, Hong M, Luo J. Effective visible-light driven CO_2 photoreduction via a promising bifunctional iridium coordination polymer. Chemical Science (Cambridge), 2014, 5(10): 3808–3813
108. Zhang S, Li L, Zhao S, Sun Z, Hong M, Luo J. Hierarchical metal–organic framework nanoflowers for effective CO_2 transformation driven by visible light. Journal of Materials Chemistry. A, 2015, 3 (30): 15764–15768
109. Zhang S, Li L, Zhao S, Sun Z, Luo J. Construction of interpenetrated ruthenium metal–organic frameworks as stable photocatalysts for CO_2 reduction. Inorganic Chemistry, 2015, 54 (17): 8375–8379
110. Lee Y, Kim S, Fei H, Kang J K, Cohen S M. Photocatalytic CO_2 reduction using visible light by metal-monocatecholato species in a metal–organic framework. Chemical Communications, 2015, 51 (92): 16549–16552
111. Chen D, Xing H, Wang C, Su Z. Highly efficient visible-light-driven CO_2 reduction to formate by a new anthracene-based zirconium MOF via dual catalytic routes. Journal of Materials Chemistry. A, 2016, 4(7): 2657–2662
112. Schaate A, Roy P, Godt A, Lippke J, Waltz F, Wiebcke M, Behrens P. Modulated synthesis of Zr-based metal–organic frameworks: from nano to single crystals. Chemistry–A European Journal, 2011, 17(24): 6643–6651
113. Gomes Silva C, Luz I, Llabrés i Xamena F X, Corma A, García H. Water stable Zr–benzenedicarboxylate metal–organic frameworks as photocatalysts for hydrogen generation. Chemistry– A European Journal, 2010, 16(36): 11133–11138
114. Cavka J H, Jakobsen S, Olsbye U, Guillou N, Lamberti C, Bordiga S, Lillerud K P. A new zirconium inorganic building brick forming metal organic frameworks with exceptional stability. Journal of the

American Chemical Society, 2008, 130(42): 13850–13851
115. Mondloch J E, Katz M J, Planas N, Semrouni D, Gagliardi L, Hupp J T, Farha O K. Are Zr_6-based MOFs water stable? Linker hydrolysis vs. capillary-force-driven channel collapse. Chemical Communications, 2014, 50(64): 8944–8946
116. Wang C C, Du X D, Li J, Guo X X, Wang P, Zhang J. Photocatalytic Cr(VI) reduction in metal-organic frameworks: a mini-review. Applied Catalysis B: Environmental, 2016, 193: 198–216
117. Dean J A. Lange's handbook of chemistry. Materials and Manufacturing Processes, 1990, 5(4): 687–688
118. Laurier K G M, Vermoortele F, Ameloot R, De Vos D E, Hofkens J, Roeffaers M B J. Iron(III)-based metal–organic frameworks as visible light photocatalysts. Journal of the American Chemical Society, 2013, 135(39): 14488–14491
119. Torrisi A, Bell R G, Mellot-Draznieks C. Functionalized MOFs for enhanced CO_2 capture. Crystal Growth & Design, 2010, 10(7): 2839–2841
120. Torrisi A, Mellot-Draznieks C, Bell R G. Impact of ligands on CO_2 adsorption in metal-organic frameworks: first principles study of the interaction of CO_2 with functionalized benzenes. II. Effect of polar and acidic substituents. Journal of Chemical Physics, 2010, 132(4): 044705
121. Tamaki Y, Morimoto T, Koike K, Ishitani O. Photocatalytic CO_2 reduction with high turnover frequency and selectivity of formic acid formation using Ru(II) multinuclear complexes. Proceedings of the National Academy of Sciences of the United States of America, 2012, 109(39): 15673–15678
122. Sato S, Morikawa T, Kajino T, Ishitani O. A highly efficient mononuclear iridium complex photocatalyst for CO_2 reduction under visible light. Angewandte Chemie International Edition, 2013, 52(3): 988–992
123. Kuramochi Y, Kamiya M, Ishida H. Photocatalytic CO_2 reduction in *N*,*N*-dimethylacetamide/water as an alternative solvent system. Inorganic Chemistry, 2014, 53(7): 3326–3332
124. Huang Z, Dong P, Zhang Y, Nie X, Wang X, Zhang X.A ZIF-8 decorated TiO_2 grid-like film with high CO_2 adsorption for CO_2 photoreduction. Journal of CO_2 Utilization, 2018, 24, 369–375
125. Cardoso J C, Stulp S, de Brito J F, Flor J B S, Frem R C G, Zanoni M V B. MOFs based on ZIF-8 deposited on TiO_2 nanotubes increase the surface adsorption of CO_2 and its photoelectrocatalytic reduction to alcohols in aqueous media. Applied Catalysis B: Environmental, 2018, 225: 563–573
126. Li R, Hu J, Deng M, Wang H, Wang X, Hu Y, Jiang H L, Jiang J, Zhang Q, Xie Y, Xiong Y. Integration of an inorganic semiconductor with a metal–organic framework: a platform for enhanced gaseous photocatalytic reactions. Advanced Materials, 2014, 26(28): 4783–4788
127. He X, Gan Z, Fisenko S, Wang D, El-Kaderi H M, Wang W N. Rapid formation of metal–organic frameworks (MOFs) based nanocomposites in microdroplets and their applications for CO_2 photoreduction. ACS Applied Materials & Interfaces, 2017, 9(11): 9688–9698
128. Wang M, Wang D, Li Z. Self-assembly of CPO-27-Mg/TiO_2 nanocomposite with enhanced performance for photocatalytic CO_2 reduction. Applied Catalysis B: Environmental, 2016, 183: 47–52
129. Crake A, Christoforidis K C, Kafizas A, Zafeiratos S, Petit C. CO_2 capture and photocatalytic reduction using bifunctional TiO_2/MOF nanocomposites under UV–vis irradiation. Applied Catalysis B: Environmental, 2017, 210: 131–140
130. Wang S, Wang X. Photocatalytic CO_2 reduction by CdS promoted with a zeolitic imidazolate framework. Applied Catalysis B: Environmental, 2015, 162: 494–500
131. Wang S, Lin J, Wang X. Semiconductor–redox catalysis promoted by metal–organic frameworks for CO_2 reduction. Physical Chemistry Chemical Physics, 2014, 16(28): 14656–14660
132. Shi L, Wang T, Zhang H, Chang K, Ye J. Electrostatic self-assembly of nanosized carbon nitride nanosheet onto a zirconium metal–organic framework for enhanced photocatalytic CO_2 reduction. Advanced Functional Materials, 2015, 25(33): 5360–5367
133. Xu G, Zhang H, Wei J, Zhang H X, Wu X, Li Y, Li C, Zhang J, Ye J. Integrating the g-C_3N_4 Nanosheet with B–H bonding decorated metal–organic framework for CO_2 activation and photoreduction. ACS Nano, 2018, 12(6): 5333–5340
134. Liu Q, Low Z X, Li L, Razmjou A, Wang K, Yao J, Wang H. ZIF-8/Zn_2GeO_4 nanorods with an enhanced CO_2 adsorption property in an aqueous medium for photocatalytic synthesis of liquid fuel. Journal of Materials Chemistry. A, 2013, 1(38): 11563–11569
135. Sun D, Liu W, Fu Y, Fang Z, Sun F, Fu X, Zhang Y, Li Z. Noble metals can have different effects on photocatalysis over metal–organic frameworks (MOFs): a case study on M/NH_2-MIL-125(Ti) (M = Pt and Au). Chemistry–A European Journal, 2014, 20(16): 4780–4788
136. Fu Y, Yang H, Du R, Tu G, Xu C, Zhang F, Fan M, Zhu W. Enhanced photocatalytic CO_2 reduction over Co-doped NH_2-MIL-125(Ti) under visible light. RSC Advances, 2017, 7(68): 42819–42825
137. Choi K M, Kim D, Rungtaweevoranit B, Trickett C A, Barmanbek J T D, Alshammari A S, Yang P, Yaghi O M. Plasmon-enhanced photocatalytic CO_2 conversion within metal–organic frameworks under visible light. Journal of the American Chemical Society, 2017, 139(1): 356–362
138. Wang X, Zhao X, Zhang D, Li G, Li H. Microwave irradiation induced UIO-66–NH_2 anchored on graphene with high activity for photocatalytic reduction of CO_2. Applied Catalysis B: Environmental, 2018, 228: 47–53
139. Sadeghi N, Sharifnia S, Do T O. Enhanced CO_2 photoreduction by a graphene–porphyrin metal–organic framework under visible light irradiation. Journal of Materials Chemistry. A, 2018, 6(37): 18031–18035
140. Pipelzadeh E, Rudolph V, Hanson G, Noble C, Wang L. Photoreduction of CO_2 on ZIF-8/TiO_2 nanocomposites in a gaseous photoreactor under pressure swing. Applied Catalysis B: Environmental, 2017, 218: 672–678
141. Chaudhary Y S, Woolerton T W, Allen C S, Warner J H, Pierce E, Ragsdale S W, Armstrong F A. Visible light-driven CO_2 reduction by enzyme coupled CdS nanocrystals. Chemical Communications, 2012, 48(1): 58–60
142. Liu B J, Torimoto T, Yoneyama H. Photocatalytic reduction of CO_2 using surface-modified CdS photocatalysts in organic solvents.

Journal of Photochemistry and Photobiology A: Chemistry, 1998, 113(1): 93–97

143. Fujiwara H, Hosokawa H, Murakoshi K, Wada Y, Yanagida S, Okada T, Kobayashi H. Effect of surface structures on photocatalytic CO_2 reduction using quantized CdS nanocrystallites. Journal of Physical Chemistry B, 1997, 101(41): 8270–8278
144. Nguyen N T, Altomare M, Yoo J, Schmuki P. Efficient photocatalytic H_2 evolution: controlled dewetting–dealloying to fabricate site-selective high-activity nanoporous Au particles on highly ordered TiO_2 nanotube arrays. Advanced Materials, 2015, 27(20): 3208–3215
145. Bouhadoun S, Guillard C, Dapozze F, Singh S, Amans D, Bouclé J, Herlin-Boime N. One step synthesis of N-doped and Au-loaded TiO_2 nanoparticles by laser pyrolysis: application in photocatalysis. Applied Catalysis B: Environmental, 2015, 174–175: 367–375
146. Wu H J, Henzie J, Lin W C, Rhodes C, Li Z, Sartorel E, Thorner J, Yang P, Groves J T. Membrane-protein binding measured with solution-phase plasmonic nanocube sensors. Nature Methods, 2012, 9(12): 91189
147. Tao A, Sinsermsuksakul P, Yang P. Polyhedral silver nanocrystals with distinct scattering signatures. Angewandte Chemie International Edition, 2006, 45(28): 4597–4601
148. Han B, Ou X, Deng Z, Song Y, Tian C, Deng H, Xu Y J, Lin Z. Nickel metal–organic framework monolayers for photoreduction of diluted CO_2: metal-node-dependent activity and selectivity. Angewandte Chemie International Edition, 2018, 57(51): 16811–16815